# Challenges in High-Fidelity Implicit Block-Based Numerical Simulation of Dynamic Out-of-Plane Two-Way Bending in Unreinforced Brick Masonry Walls

Ghezelbash, Amirhossein; Sharma, Satyadhrik; D'Altri, Antonio Maria; Lourenço, Paulo B.; Rots, Jan G.; Messali, Francesco

**DOI**
10.1002/eqe.4337

**Publication date**
2025

**Document Version**
Final published version

**Published in**
Earthquake Engineering and Structural Dynamics

*Earthquake Engineering & Structural Dynamics*

WILEY



RESEARCH ARTICLE OPEN ACCESS

# Challenges in High-Fidelity Implicit Block-Based Numerical Simulation of Dynamic Out-of-Plane Two-Way Bending in Unreinforced Brick Masonry Walls

Amirhossein Ghezelbash[1] | Satyadhrik Sharma[1] | Antonio Maria D'Altri[2] | Paulo B. Lourenço[3] | Jan G. Rots[1] | Francesco Messali[1]

[1]Faculty of Civil Engineering and Geosciences, Delft University of Technology, Delft, the Netherlands | [2]Department of Civil, Chemical, Environmental, and Materials Engineering, University of Bologna, Bologna, Italy | [3]ISISE, Department of Civil Engineering, University of Minho, Guimarães, Portugal

**Correspondence:** Amirhossein Ghezelbash (a.ghezelbash@tudelft.nl)

**Received:** 4 December 2024 | **Revised:** 24 February 2025 | **Accepted:** 1 March 2025

**Funding:** This research was conducted as part of the scientific consolidation of projects funded by Nederlandse Aardolie Maatschappij (NAM) BV under contract number UI46268 “Physicaltesting and modeling–Masonry structures Groningen,” which is gratefully acknowledged. This project has also received funding from the European Union's Horizon 2020 research and innovation programme under the Marie Sklodowska-Curie grant agreement No 101029792. This study has been also funded by the STAND4HERITAGE project (new STANDards FOR seismic assessment of built cultural HERITAGE) that has received funding from the European Research Council (ERC) under the European Union's Horizon 2020 research and innovation program (Grant No 833123) as an advanced grant.

**Keywords:** numerical modeling | out-of-plane | seismic loading | two-way bending | unreinforced masonry

## ABSTRACT

This study deals with the high-fidelity block-based finite element simulation of dynamic out-of-plane (OOP) responses of unreinforced masonry (URM) walls, explicitly focusing on two-way bending behaviors under seismic loads, which is a common critical failure mode in real-world masonry structures. While experimental shake-table tests provide valuable insights into these behaviors, their high costs, complexity, and limited scalability highlight the need for advanced numerical modeling approaches. A state-of-the-art block-based finite element modeling strategy that conceives masonry as an assemblage of 3D damaging blocks interacting via contact-based cohesive-frictional zero-thickness interfaces, previously proposed for simulating cyclic quasi-static and dynamic one-way bending tests, is here extended for the first time to the simulation of incremental dynamic shake-table tests on OOP two-way spanning URM full-scale walls, subjected to a sequence of dynamic loads. The numerical models track the reference experimental behaviors with high accuracy in terms of collapse onset, failure mechanism, experienced acceleration and displacements, and hysteretic response. The effects of variations in mechanical properties, boundary conditions, and damping on the dynamic response are explored in a sensitivity study. The results indicate that slight changes in these parameters can lead to considerable differences in outcomes. This highlights the chaotic nature of the dynamic response of masonry walls, especially in near-collapse conditions, which makes probabilistic approaches more suitable for predicting masonry OOP dynamics. The proposed numerical methodology appears compatible with statistical frameworks, given the limited costs with respect to experimental tests, and it extends knowledge beyond physical experiments.

## 1 | Introduction

Masonry structures, particularly those made of unreinforced masonry (URM), are very common around the world due to the accessibility of the material, a simple construction process, high durability, low maintenance costs, and so forth [1]. However, the high vulnerability of masonry structures to earthquake actions remains a critical issue for seismic engineering, given their wide use in regions with significant as well as moderate seismicity and the challenges in predicting their behavior [2–7]. While most research on the seismic response of URM structures focuses on in-plane loading, where forces act parallel to the wall, the out-of-plane (OOP) response is also crucial for structural stability, especially for slender walls [6, 8]. OOP failure, particularly in the case of two-way bending, presents additional complexities compared to one-way bending. Two-way bending behaviors are widely encountered in real-world buildings due to the connection of URM walls to adjacent structural components, such as pillars or return walls [9]. The OOP response of this structural configuration is particularly complex, but its study has been relatively limited in the literature [10–18].

To better understand and mitigate this vulnerability, it is essential to develop models that can reliably predict the behavior of masonry structures under dynamic loading conditions. Models for assessing the seismic response of masonry structures can be either physical or numerical. Physical models, typically tested in laboratories, provide valuable real-world data on how structures respond to earthquakes. State-of-the-art testing of URM walls under OOP two-way bending behavior is carried out in the form of quasi-static monotonic [19–23] or cyclic [24–27] pushover and dynamic shake-table [10–12] tests in the literature. Shake-table tests are particularly useful for replicating seismic loads and studying the effects of dynamic loading on the failure mechanisms, crack propagation, and load-bearing capacity.

Despite their advantages, physical models have significant limitations. They are expensive to build and operate, limiting the number of tests that can be conducted [19]. Shake-table experiments also suffer from reproducibility issues related to variations in workmanship, boundary conditions, loading sequences, or the test setup. Moreover, the boundary conditions and loading sequences used in these tests may not fully represent real-world conditions due to setup constraints [28–31]. As a result, physical models are highly specific to the tested structure, and their findings may not be generalized easily to other scenarios unless they are repeated a statistically significant number of times, which is often prohibitively expensive. Additionally, physical models can only test a limited number of cases, restricting their ability to explore the broader statistical dynamics of masonry behavior [32]. These drawbacks highlight the need for alternative methods that can complement physical experiments.

Numerical models offer a flexible and cost-effective alternative to physical testing, enabling the simulation of dynamic behavior in masonry structures under a wide range of conditions. When properly validated against benchmark experiments, their main advantage is their ability to test several scenarios at a fraction of the costs and time of physical tests, allowing for comprehensive statistical investigations of masonry dynamics under different loading conditions. Additionally, numerical models offer greater freedom in representing complex boundary conditions and structural configurations that are difficult to replicate in a laboratory. They can also simulate full-scale structures, a critical point in dynamics, without being constrained by specimen size. A variety of numerical models are available, ranging from simplified macro-element [13, 14, 33] and continuum-based [34–38] models to multi-scale [39] and more detailed block-based ones [40–43]. Macro-element models are computationally efficient and useful for large-scale seismic assessments but fail to account for localized (material-scale) effects of cracking and crushing, which are critical for understanding failure mechanism evolution [44]. Continuum-based and multi-scale models can theoretically account for these effects, yet the calibration of their constitutive behaviors is not typically straightforward and often requires adjustment at different levels [44]. In contrast, block-based models, within the discrete element [45], the finite element [46, 47], and the advanced element [15] frameworks, simulate masonry at the unit level, providing a detailed representation of blocks and joints. These models rely on solid mechanical hypotheses to accurately represent failure mechanisms such as joint cracking and shearing and unit crushing and splitting, being, therefore, able to capture both global behavior and localized failures with high fidelity [44], especially in near-collapse and collapse scenarios. However, these models have rarely been used to simulate full-scale OOP behaviors in a dynamic framework, plausibly due to large computational demands. Moreover, they require careful calibration and then validation against physical experiments to ensure their reliability in extending the current knowledge.

To address the knowledge gaps mentioned, this study investigates the dynamic OOP two-way bending responses in URM walls via a robust high-fidelity computational modeling framework. A state-of-the-art damaging block-based finite element model, which conceives masonry as an assemblage of 3D damaging expanded blocks interacting via contact-based cohesive-frictional zero-thickness interfaces, originally proposed for cyclic quasi-static simulations [48], has been recently extended in [49] for dynamic analysis of OOP one-way bending responses. A simplified mechanical characterization for the nonlinear response of blocks and joints was proposed for improved efficiency in wall-level analyses. Dynamic simulation was made possible using a generalized HHT-$\alpha$ (Hilbert Hughes Taylor) direct integration implicit solver and by implementing Rayleigh damping in the expanded blocks. This combination allowed the use of both mass and stiffness proportional damping without affecting the simulation time. The modeling approach was validated against a full-scale experiment on a one-way spanning single-leaf calcium silicate wall under incremental dynamic shake table loading [50]. The numerical model accurately captured the response of the experiment in terms of collapse onset, failure mechanism, experienced accelerations and displacements, hysteretic response, and energy dissipation.

This study builds on the previous work by focusing on the more complex OOP two-way bending behaviors and furthering the current knowledge base to scenarios that are not studied experimentally. The proposed numerical modeling strategy is employed to replicate the outcomes of the incremental dynamic shake table tests performed by Graziotti et al. [11] on single-leaf two-way spanning calcium silicate URM walls. Only two prior studies [15, 39] have attempted detailed numerical simulation of dynamic OOP experiments on unreinforced masonry walls, such as the tests [11] used in this study. One of these studies [39] approximates the dynamic response through a simplified pushover loading approach, which does not allow for a point-by-point comparison between numerical and experimental observations. The other study [15] conducts dynamic analysis with a simplified loading sequence and exhibits mismatches with experimental outcomes, as will be discussed in the manuscript. Hence, current publication marks one of the few and first instances where they are successfully modeled up to collapse via a high-fidelity 3D block-based approach and with their entire multi-step dynamic loading sequencies considered. The experimental specimens selected for model validation, introduced in Section 2, cover different boundary conditions and geometries. The wide range of responses these walls exhibit is simulated by considering a consistent set of assumptions for the boundary conditions, loading protocol, mechanical parameters, and solver settings, avoiding the specimen-specific adjustment of modeling parameters. Section 3 details the modeling procedure. Section 4 compares the results of the simulations to the experimental data, evaluating the effectiveness of the modeling strategy and highlighting the challenges encountered in the simulation process. A sensitivity study, presented in Section 5, explores how variations applied to mechanical properties, boundary conditions, and damping affect the dynamic response, offering insights into potential experimental variations and checking the appropriateness of the block-based finite element modeling assumptions. Such variations can also be considered as the extrapolation of the current experimental findings to scenarios that could have been observed had the experiments gone slightly differently. The study concludes in Section 6 with a discussion of the findings and future research directions.

## 2 | Reference Experimental Tests

The experiments of Graziotti et al. [11] on URM walls subjected to OOP seismic loading are used to validate the proposed modeling strategy and to carry out the subsequent sensitivity studies. The experimental campaign, conducted at EUCENTRE Foundation in Pavia, Italy, contains several tests on single- and multi-leaf one- and two-way spanning walls under shake table loading [50–53]. Three tests on two-way spanning single-leaf calcium silicate return walls with distinct boundary conditions and geometries (see Section 2.1) are simulated. These tests are selected because (1) the experimental campaign covers the behavior of masonry constructions at different levels, from small-scale material characterization to dynamic testing of buildings [54], providing the data necessary for the calculation of the numerical input parameters, and (2) they are among the most advanced studies on the effects of geometry and boundary conditions on the OOP response, offering the most comprehensive benchmarks to assess the applicability of the proposed modeling strategy over a wide range of structures. This section reports the key features of the experimental specimens in terms of geometry, boundary conditions, and testing procedure.

### 2.1 | Geometry

The experimental specimens simulated in this study consist of a three-sides supported wall without an opening with a free top edge, a similarly supported wall with a window opening, and another no-opening wall supported at all its four edges. The walls are indicated as CS-000-RF, CSW-000-RF, and CS-005-RR/CS-010-RR in the reference publication [11], respectively, and are referred to as 3SS (3-side supported solid), 3SO (3-side supported opening), and 4SS (4-side supported solid) walls in this study. Figure 1 provides an overview of the specimens and their geometrical dimensions. Each wall is 275.4 cm high and 397.8 cm long, connected to 99.4 cm perpendicular return elements (referred to as “flanges” in the text) at each end. The window opening in the 3SO wall is 177.6 cm long and 162.0 cm high. It is positioned at a 154.5 cm distance from the left edge of the wall and a 56.7 cm distance from the base, giving the wall an asymmetric geometry. All three walls are constructed with 34 courses of $21.2 \times 7.1 \times 10.2$ cm (length × height × thickness) solid calcium silicate bricks, assembled in running bond layup using 1.0 cm thick multipurpose M5 mortar layers. For the 3SO wall, a $199.8 \times 16.2 \times 10.2$ cm (length × height × thickness) concrete lintel is placed above the window opening and is connected to the rest of the wall via regular mortar. No window frame is considered inside the opening.

### 2.2 | Test Set-Up

The test set-up shown in Figure 1a,b is used in the experiments to apply the dynamic excitation at the boundaries of each wall. The base of the walls is placed on a pre-stressed reinforced concrete foundation fixed to the shaking table via steel bolts. Regular mortar is used between the lower-most brick course and the foundation. A rigid steel frame transfers the dynamic motion of the shake table to the top of the walls with almost no amplification effect on the input signal. The frame is connected to the top of the walls via a rigid steel beam placed on the topmost course of bricks. The hinge system shown in Figure 2a connects the frame to the beam. It is made of four steel braces pinned to the frame via cylindrical hinges and fully fixed to the beam, allowing uplift as well as rotation of the beam around the in-plane axis (of the main wall) with no relative rotation of the beam with respect to the steel braces. The dynamic motion is transferred to the flanges via L-shaped steel profiles assembled to enclose the top brick course of each flange (except for the corner bricks) and to connect to the steel beam via steel plates and the bolting system shown in Figure 2b. In the 4SS wall, the top beam rests on the wall and is fully clamped to the top brick course via high-strength mortar and the L-shape profiles shown in Figure 2c. In contrast, a 30 mm gap is maintained between the beam and the top of 3SS and 3SO walls to create the top-free boundary conditions. Accordingly, steel spacers are used to establish the beam-flange connections, as Figure 2d,e shows. A steel assembly is used at the back of each flange (from the bottom to four brick courses beneath the top) to restrain their lateral movement while allowing uplift and rotation around the in-plane axis (of the main wall), as Figure 2f shows. A compressive force is applied to the top of the walls via the vertical spring system shown in the same figure. The stiffness of the spring adopted ensures that the compressive force remains almost constant during the seismic tests. In fact, this force was

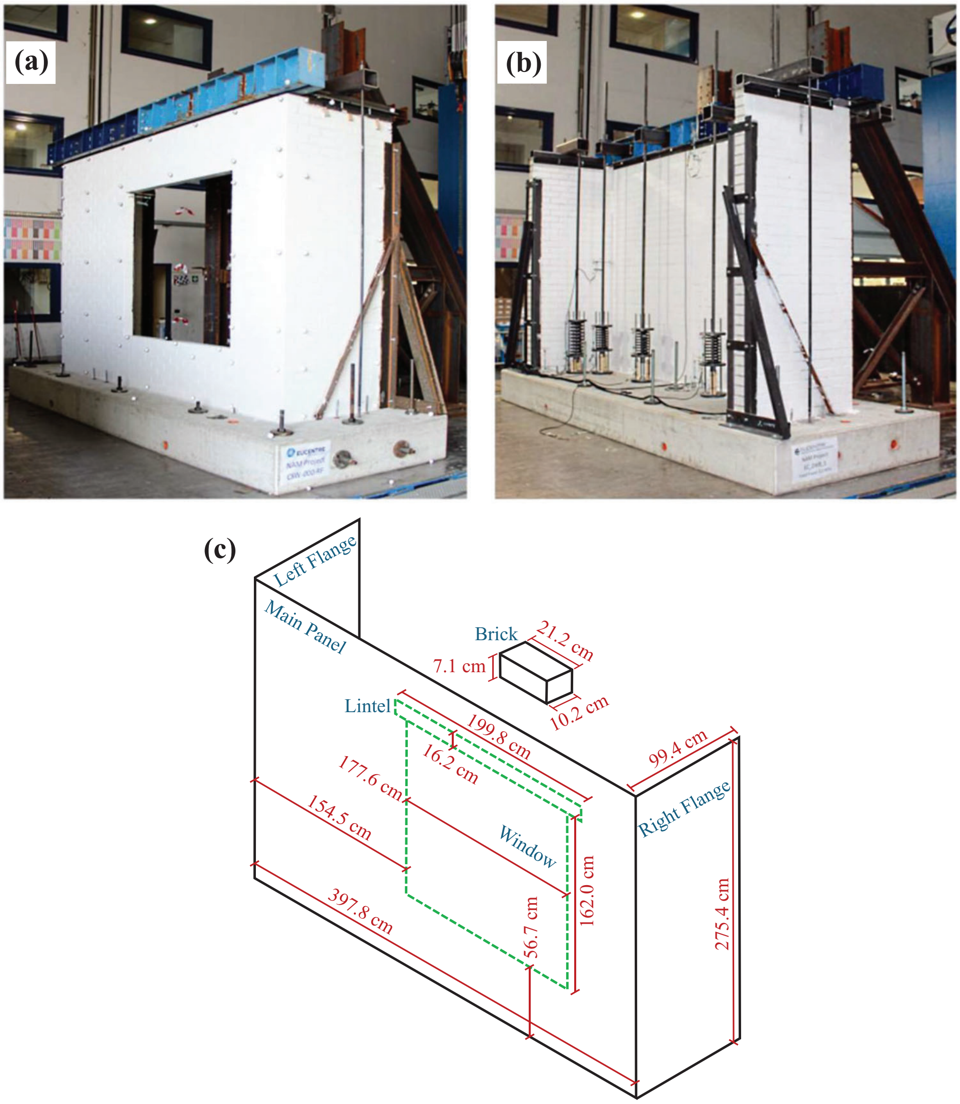


**FIGURE 1** | Overview and geometry of the two-way-bending benchmark experimental walls [55]: overview of the 3SS/4SS walls (a) and the 3SO wall (b), and geometrical dimensions (c). In the drawing, the lintel and the window, highlighted with green dashed lines, belong to the 3SO wall only.

monitored to vary only by a maximum of 5% of the initial static pre-compression. It should be noted that while the entire top of the 4SS wall (main panel and flanges) is pre-compressed, the vertical load in the 3SS and 3SO walls is only applied to the top of the flanges, preventing any confinement at the top of the main walls. Hence, the springs connected to the main panel of the 4SS wall, shown in Figure 2f, are replaced by vertical jacks in 3SS and 3SO walls to establish the previously maintained beam-wall gap, as Figure 2a shows.

## 2.3 | Loading Sequence

Each wall is subjected to multiple dynamic loading steps (or runs). The intensity of the motions is incrementally increased from each run to the next until collapse is reached. Figure 3 shows the acceleration time histories and the spectral acceleration and displacement data of the reference signals used in the experimental study. The FHUIZ-DS0 signal is the second-floor acceleration time history obtained from the numerical model of a two-story URM building subjected to the Huizinge event ground motion at its base [56]. The Huizinge induced-seismicity earthquake, which occurred on April 16, 2012, represents the largest earthquake event in the Groningen province of the Netherlands until the experiments of Graziotti et al. [11] were being carried out. Signals FEQ2-DS3 and FEQ2-DS4 are the second-floor acceleration time histories recorded during the shake table testing of a two-story URM building subjected to incremental dynamic loading [57]. The input ground motion used in the reference building experiment has been obtained from a hazard study conducted in 2015 [58]. It represents an induced-seismicity event with an associated PGA of 0.16 g in the Groningen area. The two FEQ2 signals are recorded during different loading runs of the building experiment with different levels of damage observed in the building. FEQ2-DS3 is the floor acceleration when moderate (damage state 3/DS3) damages have been observed in the building. FEQ2-DS4 is the acceleration of the same floor recorded when the building reached near-collapse (damage state 4/DS4) conditions. The signals introduced above had not been able to push the 4SS wall to collapse. Hence, a fourth record is

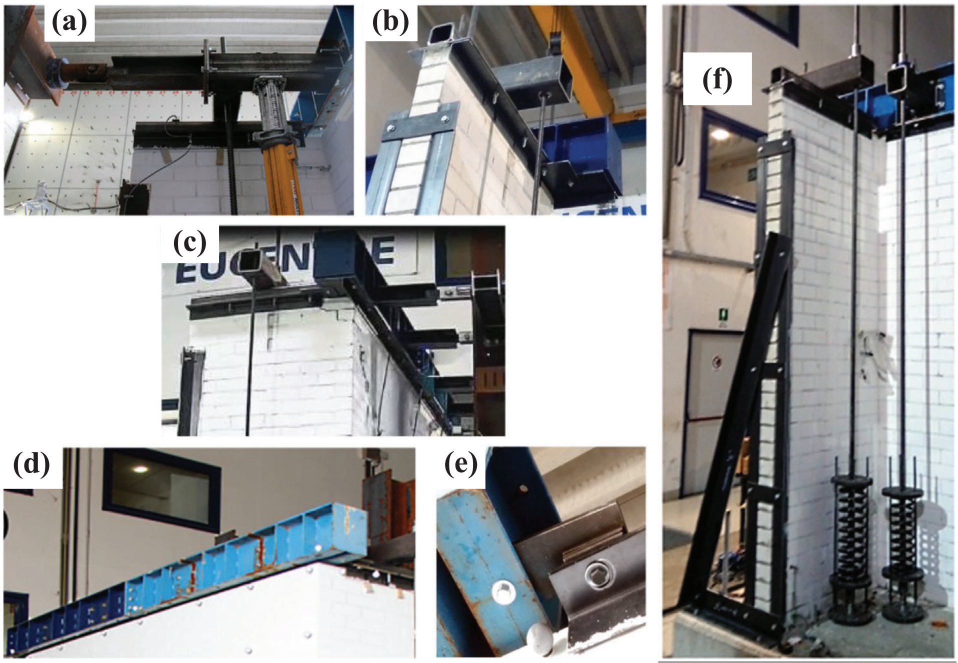


FIGURE 2 | Test set-up of the two-way-bending benchmark experiments [55]: frame/beam hinge connection (a), beam/flange connection (b), beam connection to 4SS wall (c), beam/wall connection (d), beam/flange spacers in 3SS/3SO walls (e), and vertical loading springs (f).

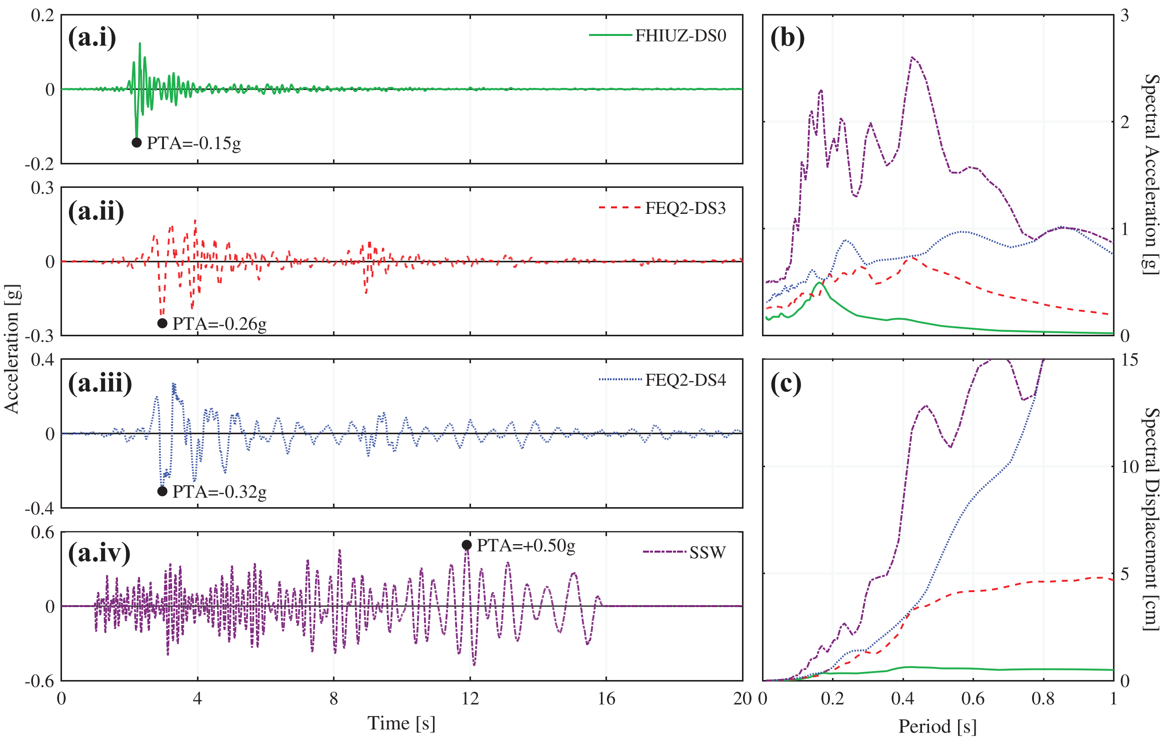


FIGURE 3 | Overview of the loading input signals used in the testing of the experimental benchmark [11]: acceleration time histories (a), and 5%-damped acceleration (b) and displacement spectra (c).

adopted for this specimen. This record is indicated as SSW and consists of a 20-s artificial acceleration time history generated using a sequence of sine impulses with gradually increasing periods. The wide spectral shape of the signal has allowed it to excite the wall in all frequency ranges without the need to scale the load to unrealistically high intensities.

Table 1 provides the detailed loading sequence of each specimen. The 3SS, 3SO, and 4SS walls are subjected to 31, 22, and 27 loading runs, respectively. This has allowed Graziotti et al. [11] to extract the maximum amount of information from a single test, achieving a detailed characterization of the OOP response of the specimens both in the undamaged elastic regime and under the influence

**TABLE 1** | Loading sequence adopted in the testing of the experimental benchmarks [11].

| **3SS wall** | | | | **3SO wall** | | | | **4SS wall** | | | |
|---|---|---|---|---|---|---|---|---|---|---|---|
| **Run #** | **Input** | **Scale** | **PTA* [g]** | **Run #** | **Input** | **Scale** | **PTA* [g]** | **Run #** | **Input** | **Scale** | **PTA* [g]** |
| 0.05 MPa vertical compression (flanges) | | | | 0.05 MPa vertical compression (flanges) | | | | 0.1 MPa vertical compression (entire wall) | | | |
| 1 | RN | — | — | 1 | RN | — | — | 1 | RN | — | — |
| 2 | FHUIZ-DS0 | 50% | −0.07 | 2 | RN | — | — | 2 | FHUIZ-DS0 | 50% | −0.07 |
| 3 | FHUIZ-DS0 | 100% | −0.15 | 3 | FHUIZ-DS0 | 50% | −0.07 | 3 | FHUIZ-DS0 | 100% | −0.16 |
| 4 | FHUIZ-DS0 | 150% | −0.23 | 4 | FHUIZ-DS0 | 100% | −0.16 | 4 | FHUIZ-DS0 | 150% | −0.20 |
| 5 | RN | — | — | 5 | FHUIZ-DS0 | 150% | −0.22 | 5 | FEQ2-DS3 | 40% | −0.11 |
| 6 | FEQ2-DS3 | 50% | −0.16 | 6 | FEQ2-DS3 | 50% | −0.13 | 6 | FEQ2-DS3 | 89% | −0.22 |
| 7 | FEQ2-DS3 | 89% | −0.23 | 7 | FEQ2-DS3 | 89% | −0.25 | 7 | FEQ2-DS3 | 100% | −0.27 |
| 8 | FEQ2-DS3 | 100% | −0.25 | 8 | FEQ2-DS3 | 100% | −0.27 | 8 | FEQ2-DS3 | 125% | −0.31 |
| 9 | FEQ2-DS3 | 125% | −0.34 | 9 | FEQ2-DS3 | 125% | −0.31 | 9 | RN | — | — |
| 10 | FEQ2-DS4 | 100% | −0.39 | 10 | RN | — | — | 10 | RWA | 100% | +0.30 |
| 11 | FEQ2-DS4 | 125% | −0.38 | 11 | FEQ2-DS4 | 50% | −0.16 | 11 | FEQ2-DS4 | 50% | −0.17 |
| 12 | FEQ2-DS4 | 150% | −0.46 | 12 | FEQ2-DS4 | 100% | −0.30 | 12 | FEQ2-DS4 | 100% | −0.32 |
| 13 | FEQ2-DS4 | 175% | −0.54 | 13 | FEQ2-DS4 | 125% | −0.39 | 13 | FEQ2-DS4 | 125% | −0.38 |
| 14 | FEQ2-DS4 | 200% | −0.68 | 14 | FEQ2-DS4 | 150% | −0.45 | 14 | FEQ2-DS4 | 150% | −0.47 |
| 15 | FEQ2-DS4 | 250% | −0.78 | 15 | FEQ2-DS4 | 175% | −0.53 | 15 | FEQ2-DS4 | 200% | −0.74 |
| 16 | FEQ2-DS4 | 300% | −0.95 | 16 | FEQ2-DS4 | 200% | −0.65 | 16 | FEQ2-DS4 | 250% | −0.91 |
| 17 | FEQ2-DS4 | 350% | −1.10 | 17 | FEQ2-DS4 | 250% | −0.81 | 17 | FEQ2-DS4 | 300% | −0.90 |
| **18** | **FEQ2-DS4** | **400%** | **−1.28** | 18 | FEQ2-DS4 | 300% | −0.91 | vertical compression reduced to 0.05 MPa | | | |
| 19 | RN | — | — | 19 | FEQ2-DS4 | 350% | −1.13 | 18 | FEQ2-DS4 | 100% | −0.32 |
| 20 | FHUIZ-DS0 | 100% | −0.15 | **20** | **FEQ2-DS4** | **400%** | **−1.28** | 19 | FEQ2-DS4 | 200% | −0.64 |
| 21 | FEQ2-DS3 | 100% | −0.24 | 21 | RN | — | — | 20 | FEQ2-DS4 | 300% | −1.05 |
| 22 | FEQ2-DS4 | 200% | −0.62 | 22 | FHUIZ-DS0 | 100% | −0.15 | 21 | FEQ2-DS4 | 400% | −1.18 |
| | | | | 23 | FEQ2-DS3 | 100% | −0.25 | **22** | **FEQ2-DS4** | **600%** | **−1.93** |
| | | | | 24 | FEQ2-DS4 | 100% | −0.33 | 23 | RN | — | — |
| | | | | 25 | FEQ2-DS4 | 150% | −0.46 | 24 | SSW×2 | 75% | +0.38 |
| | | | | 26 | FEQ2-DS4 | 200% | −0.78 | 25 | SSW×2 | 200% | +0.99 |
| | | | | 27 | FEQ2-DS4 | 300% | −0.91 | 26 | SSW×2 | 250% | +1.39 |
| | | | | | | | | 27 | RN | — | — |
| | | | | | | | | 28 | SSW×2 | 150% | +0.92 |
| | | | | | | | | 29 | SSW×2 | 150% | +0.81 |
| | | | | | | | | 30 | SSW×2 | 100% | +0.66 |
| | | | | | | | | 31 | SSW | 300% | +1.42 |

*Recorded peak table acceleration.

*Note:* Loading runs highlighted in bold are those after which the first cracks of each wall specimen are observed during visual inspection.

of damages accumulated during preceding loading runs. This helps to simulate real-world conditions where pre-existing damage from previous loading events can potentially influence the behavior of the walls. The loading runs are carried out back-to-back without repositioning the specimen to its original resting (no-displacement) conditions. Moreover, the signals of Figure 3 are scaled to different intensities for each loading run via the factors reported in Table 1, leading to the recorded peak shake table accelerations (PTAs) listed in the table. The sign of the PTAs indicates the direction in which the PTA is recorded: a negative sign means the PTA points toward the face of the wall (where the flanges start), while a positive sign aligns with the flanges, pointing in the direction they extend. For the 3SS and 3SO walls, a 0.05 MPa pre-compression is applied as vertical loading to the flanges and maintained constant during the dynamic loading runs. In contrast, the 4SS wall is first subjected to a 0.1 MPa pre-compression at its entire top surface until loading run 17, and then the vertical load is reduced to 0.05 MPa from run 18 forward.

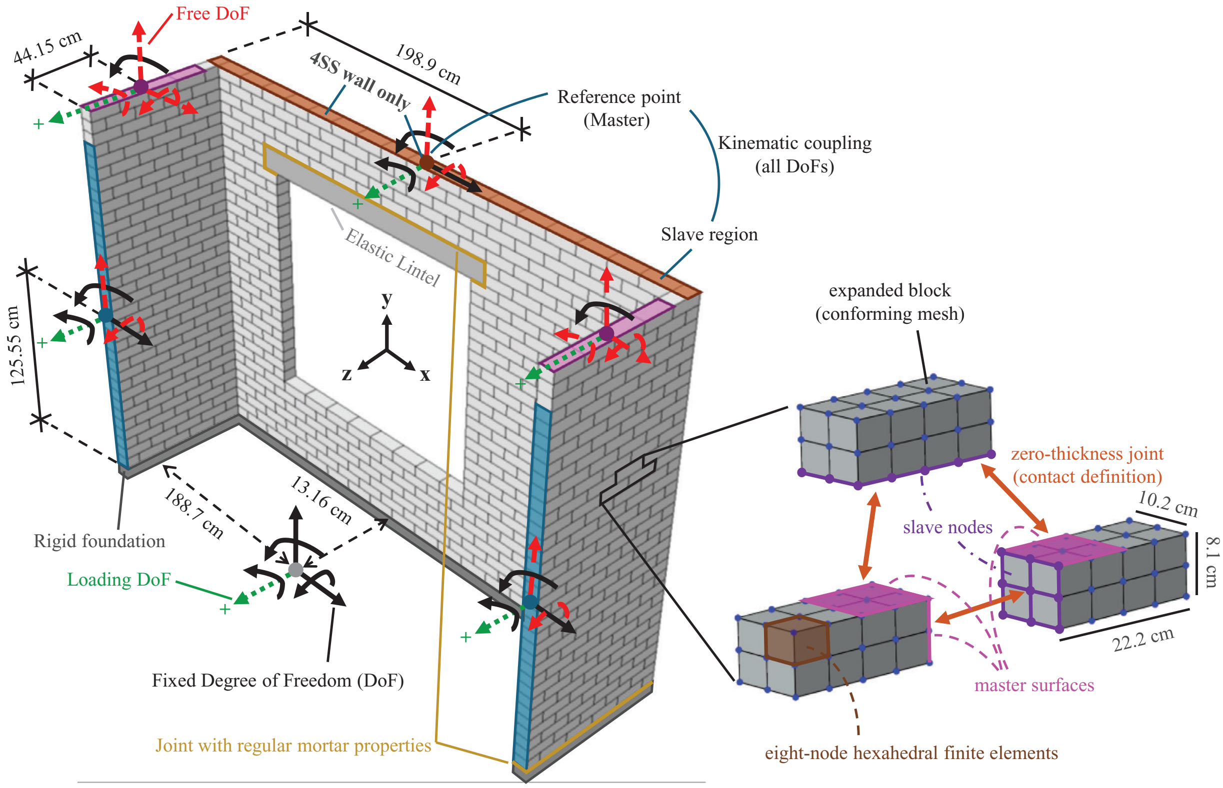


**FIGURE 4** | Geometry, discretization, and boundary conditions of the numerical models.

Low amplitude random noise (indicated as RN) excitation is used at the start of the experiments and between different loading runs to obtain the natural frequency of the first vibration mode of the specimens and to check the changes in the stiffness as a consequence of damage accumulations. Bold text is used in Table 1 to highlight the loading run, after which the first cracks of each specimen are observed through visual inspection. The collapse of each specimen has occurred during its last reported loading run either in the form of loss of stability (3SS and 4SS walls) or excessive cracking (3SO wall). The “SSW×2” in the loading runs 24 and beyond in the 4SS wall indicates that the SSW signal has been applied two times in each run, without rest time between the motions. A 2 Hz Ricker Wavelet, indicated with RWA, is also used for the 4SS wall.

## 3 | Numerical Modeling of The Reference Experiments

The 3D damaging block-based numerical modeling strategy developed in [48] for quasi-static cyclic loading and extended to dynamics in [49] has been employed. This section briefly describes the relevant points of the numerical modeling strategy and the specific considerations made for the simulation of the benchmark experiments introduced in Section 2. The reader is referred to publications [48, 49] for further details.

### 3.1 | Geometry and Boundary Conditions

Figure 4 presents the geometry and the boundary conditions in the two-way spanning numerical models considered in this study. Specifically, the 3SO wall is illustrated as it presents the most complex geometrical details among the three walls. The geometry of the masonry is represented unit-by-unit via zero-thickness joints and three-dimensional expanded blocks: each block is expanded in height and length by 10 mm to account for the thickness of the horizontal (bed) and vertical (head) mortar layers, resulting in 22.2 × 8.1 × 10.2 cm (length × height × thickness) dimensions (see Figure 1c). Each expanded block is discretized into 16 eight-node hexahedral solid finite elements with a 4 × 2 × 2 (length × height × thickness) distribution according to Figure 4. Masonry joints are idealized as zero-thickness planar contact-based cohesive-frictional interfaces. A contact algorithm using a master-slave formulation that connects each point on the slave surface to several points on the master surface is employed. The main walls are assembled in the $x$-$y$ plane, with the $y$-axis representing the vertical direction and pointing toward the top of the wall. The flanges are assumed to extend along the $z$-axis in the negative-to-positive direction.

For simplicity, the boundary conditions are directly applied to the extremities of the specimen, and the test set-up is not included in the simulation. This assumption is supported by high-strength mortar and clamping profiles to connect the walls to different parts of the test set-up in the original experiments and by the absence of any damage at the wall-frame connections reported during the tests. Nevertheless, a semi-rigid foundation is placed below the walls in order to include the lowermost mortar layer and the potential failures that can occur at the wall-foundation connection. To simplify the application of base constraints and the post-processing of the quantitative outcomes, the entire foundation is connected to a reference point placed at its geometrical center (with a 14.06 cm offset in the $z$-direction from the side of the foundation) and restricted in all degrees of freedom (DoFs). Kinematic coupling in all DoFs connects the foundation to the reference point [59]. A similar simplification is considered at the back of the flanges, where the surface of the end bricks (except the three topmost brick courses) for each flange is connected to a reference point at their mid-height (125.55 cm from the base mortar joint), for which all DoFs except uplift and rotation around $x$-axis are constrained. The top surface of each flange (except for the corner bricks) is also connected to a reference point at its mid-length (44.15 cm distance from the back of the flange in the z-direction) to simulate the rigidity of the clamping profiles used in the experiment. Here, the experimental footage showed complex behavior at the flange-top boundaries. Because the flange-beam connections in the experiments could not fully clamp the flanges, the movement of the top of the flanges has not been fully restricted, making it difficult and time-consuming to set accurate numerical boundary conditions. Hence, it is assumed that the flange-top reference points are free in all DoFs except for rotation around the $y$-axis, preventing the torsion of the flanges around the vertical direction. In addition to the explained boundary conditions, the top surface of the main wall in the 4SS and half of the corner bricks aligning with the main wall are connected to a reference point at its center, which was only allowed to uplift in the $y$-direction and rotate around the $x$-axis freely.

## 3.2 | Loading Procedure

The self-weight load is applied through constant gravitational acceleration (9.81 m/s$^2$). A constant vertical pressure is subsequently applied to the top surface of the walls (in the case of 3SS and 3SO walls, only to the flanges) following the magnitudes used in the experiments. The entire loading sequences in Table 1 are applied, excluding the random noise runs to reduce simulation time. Modal analysis is performed at the start of the simulations and after each loading run to track the evolution of the natural frequencies of the walls and to identify the onset and progression of damages. The possibility of simplifying the loading sequence for each wall is investigated in Section 5.1. Rather than using the input signals reported in Section 2.3, the dynamic simulations are performed using the acceleration data recorded at the base of the walls, allowing the numerical loadings to closely match the experimental ones. Hence, the base accelerogram recorded in each loading run is applied to the z-direction translation DoF (see Figure 4) of all boundary reference points in the numerical models. The loading signals are applied to the wall in the same directions as those used during the experiments. Applying a similar input motion to all boundaries assumes that no amplification occurred during the transfer of the motion to different parts of the specimens during the experimental campaign. All the recorded signals are used without cropping out their low-amplitude portions. However, they are cleaned from the electrical noises imposed by the experimental data acquisition instruments using a fourth-order Butterworth bandpass filtering between the 0.1 to 50 Hz frequency range [60].

## 3.3 | Mechanical Behavior Calibration

The mechanical behavior of the expanded blocks is nonlinear and modeled by means of the concrete damaged plasticity (CDP) constitutive model developed in [61] and extended in [62]. Compressive crushing and tensile cracking are assumed as the two main failure mechanisms of the expanded blocks, reproducing the response of masonry assemblies under compression and masonry units under tension, respectively. A contact-based formulation is adopted for masonry joints, idealized as zero-thickness cohesive-frictional interfaces, obeying a Mohr–Coulomb yield surface with tension cut-off to couple the shear and tensile responses in the joints, and no compressive cap. Dilatancy effects are considered in the behavior of the expanded blocks via a non-associative flow rule, and while joints are controlled by a non-dilatant behavior.

The main feature of the constitutive assumptions for the expanded blocks and joints is depicted in Figure 5. The behaviors are expressed in a simplified manner to reach a compromise between simulation speed and accuracy. In the monotonic uniaxial stress-strain response of the expanded blocks (Figure 5a), a post-peak compressive plateau is assumed, and tensile and compressive softening behaviors are formulated via linear functions. A 10% post-softening residual strength is considered for the expanded blocks to avoid numerical divergence. The uniaxial response of the blocks is projected onto a three-dimensional space via the Drucker–Prager type multi-yield surface [62]. The cyclic nonlinear behavior of the expanded blocks is characterized by elastic unloading-reloading in the compressive plateau regime and reduced-stiffness unloading-reloading during both compressive and tensile softening. The compressive and tensile behaviors of the expanded blocks are coupled in this study, meaning that prior tensile damages are assumed to reduce the compressive strength and stiffness, and vice versa. More details of the cyclic behaviors of the expanded blocks and joints can be found in [49].

The stress-displacement response of the joints is characterized by post-peak linear softening in both shear-cohesion (blue curve, Figure 5b) and tension (red curve, Figure 5c), as well as a constant shear-friction (green curve, Figure 5b). Secant unloading and reloading toward the origin point is considered for the normal response, and the overall shear response is governed by elastic cyclic stiffness. The shear response of the joints is assumed isotropic in their plane, defined based on the vectorial summations of stresses (and slipping) in the longitudinal (Vector 1, Figure 5b) and transverse (Vector 2, Figure 5b) directions, producing a three-dimensional behavior.

The values of Table 2 are used to characterize the mechanical behavior of the expanded blocks and the joints, that is, for the input parameters highlighted in Figure 5. For the expanded blocks, these include the elastic modulus $E_{\mathrm{m}}$, the strength of masonry wallets in compression ($f'_{\mathrm{m}}$), the lengths of the compressive plateau and softening branches ($\varepsilon_{\mathrm{mh}}$ and $\varepsilon_{\mathrm{mk}}$), and the tensile strength of masonry units ($f_{\mathrm{bt}}$) and the length of the tensile softening regime ($\varepsilon_{\mathrm{btk}}$). For the joints, they include the overclosure stiffness ($k_{\mathrm{no}}$), stiffness of cohesive tensile and shear responses ($k_{\mathrm{nt}}$ and $k_{\mathrm{s}}$), the elastic slip controlling the development of the shear-frictional response and the slope of the friction loading-unloading branch ($\delta_{\mathrm{e}}$), tensile and shear-cohesive strength of the mortar layers and unit-mortar interface ($f_{\mathrm{t}}$ and $c$), friction coefficient ($\tan\phi$), and the length of the tensile and shear softening responses ($u_{\mathrm{k}}$ and $\delta_{\mathrm{k}}$).

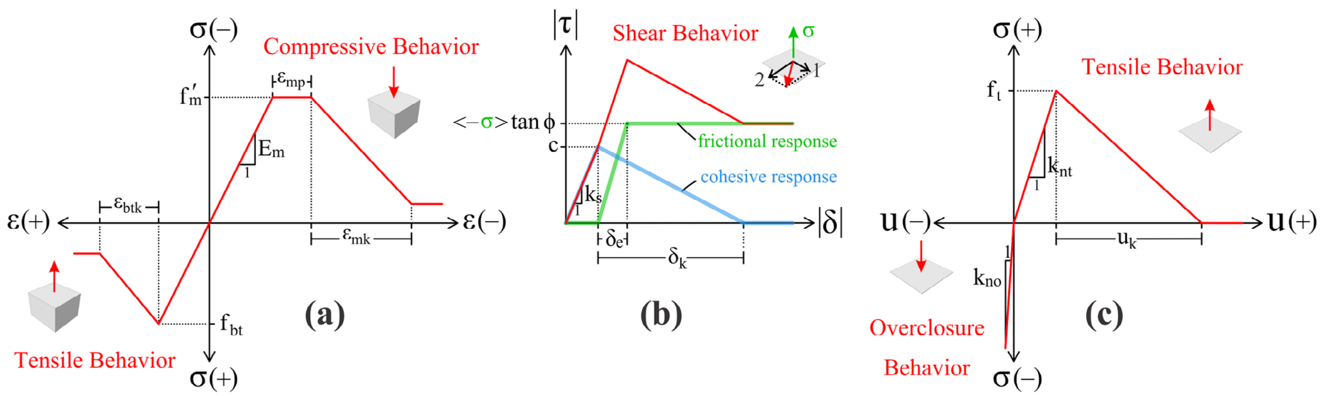


**FIGURE 5** | Constitutive material behaviors considered in the numerical model: uniaxial response of the expanded blocks (a) and shear (b) and tensile (c) response of the zero-thickness joints. Cyclic behaviors are detailed in [49].

**TABLE 2** | Input parameters for the mechanical characterization of the numerical model.

| **Expanded blocks** | | | | | | | |
|---|---|---|---|---|---|---|---|
| **Elastic behavior** | | **CDP parameters** | | **Compressive behavior** | | **Tensile behavior** | |
| $E_m$ [MPa] | 6460 | $\psi$ [°] | 10 | $f'_m$ [MPa] | 9.5 | $f_{bt}$ [MPa] | 0.9 |
| $\nu_m$ [−] | 0.17 | $\epsilon$ [−] | 0.1 | $\varepsilon_{mp}$ [−] | 0.002 | $\varepsilon_{btk}$ [−] | $7.5 \times 10^{-4}$ |
| Density [kg/m$^3$] | 1850 | $f_{b0}/f_{c0}$ [−] | 1.16 | $\varepsilon_{mk}$ [−] | 0.012 | | |
| | | $\rho$ [−] | 2/3 | | | | |
| **Zero-thickness masonry joints** | | | | | | | |
| **Overclosure behavior** | | **Tensile cohesive behavior** | | **Shear cohesive behavior** | | **Shear frictional behavior** | |
| $k_{no}$ [N/mm$^3$] | 241 | $k_{nt}$ [N/mm$^3$] | 241 | $k_s$ [N/mm$^3$] | 103.1 | $\tan\phi$ [−] | 0.58 |
| | | $f_t$ [MPa] | 0.12 | $c$ [MPa] | 0.17 | $\delta_e$ [mm] | 0.001 |
| | | $u_k$ [mm] | 0.4 | $\delta_k$ [mm] | 0.4 | | |

The approach proposed in [48] is adopted for the mechanical characterization of the expanded blocks and joints. The approach involves directly using small-scale tests conducted on the materials used to construct the walls to calibrate the mechanical input parameters described above. Additionally, input parameters for the expanded blocks, including the Poisson's ratio ($\nu_m$) and dilatancy angle ($\psi$) of the masonry and the remaining CDP parameters, are assigned typical values used for quasi-brittle material such as masonry [61, 63–65]. Since the Young's modulus in the expanded blocks ($E_m$) already represents the elastic response of masonry, the overclosure stiffness in the joints ($k_{no}$) is set to a large value to prevent block interpenetration. The length of the softening phases in the response of the blocks and the joints is calibrated (for the adopted discretization size) to represent the fracture energy of the corresponding failure mechanisms they represent. For simplicity, the length of the tensile and shear softening responses in the joints ($u_k$ and $\delta_k$) are assumed equal, and the normal stiffness in tension ($k_{nt}$) is set equal to its overclosure stiffness ($k_{no}$). Since the vertical mortar layers were filled during the construction of the experimental specimens, the head and bed joints in the numerical models are assigned the same material properties, with no distinction between them, assuming that the head joints are as strong as the bed joints. The lintel beam in the 4SO wall is assigned the same elastic properties and density as the expanded blocks. Finally, the joints between the foundations and the walls, as well as the joints surrounding the lintel beam, are given the same material properties as the regular mortar joints.

## 3.4 | Dynamic Analysis Framework

Dynamic analyses are conducted via an implicit Hilbert-Hugh-Taylor (HHT) direct integration solver with automatic time-stepping incrementation [66]. Following the methodology previously introduced in [49], the dynamic solver is used with $\alpha_{HHT} = -0.05$, and a small maximum allowed increment size ($\Delta t_{max}$) equal to the sampling interval is used for the recordings of the experimental sensors (0.00391 s). This setting was shown to introduce almost no numerical dissipation of the kinetic energy. Instead, dynamic energy dissipation is introduced by using Rayleigh damping in the expanded blocks. Both mass and stiffness proportional terms of the Rayleigh damping are utilized. A 5% damping ratio ($\zeta_R$), which performed adequately well in the simulations of the one-way spanning walls, is adopted here also for the simulation of the two-way spanning walls, while the

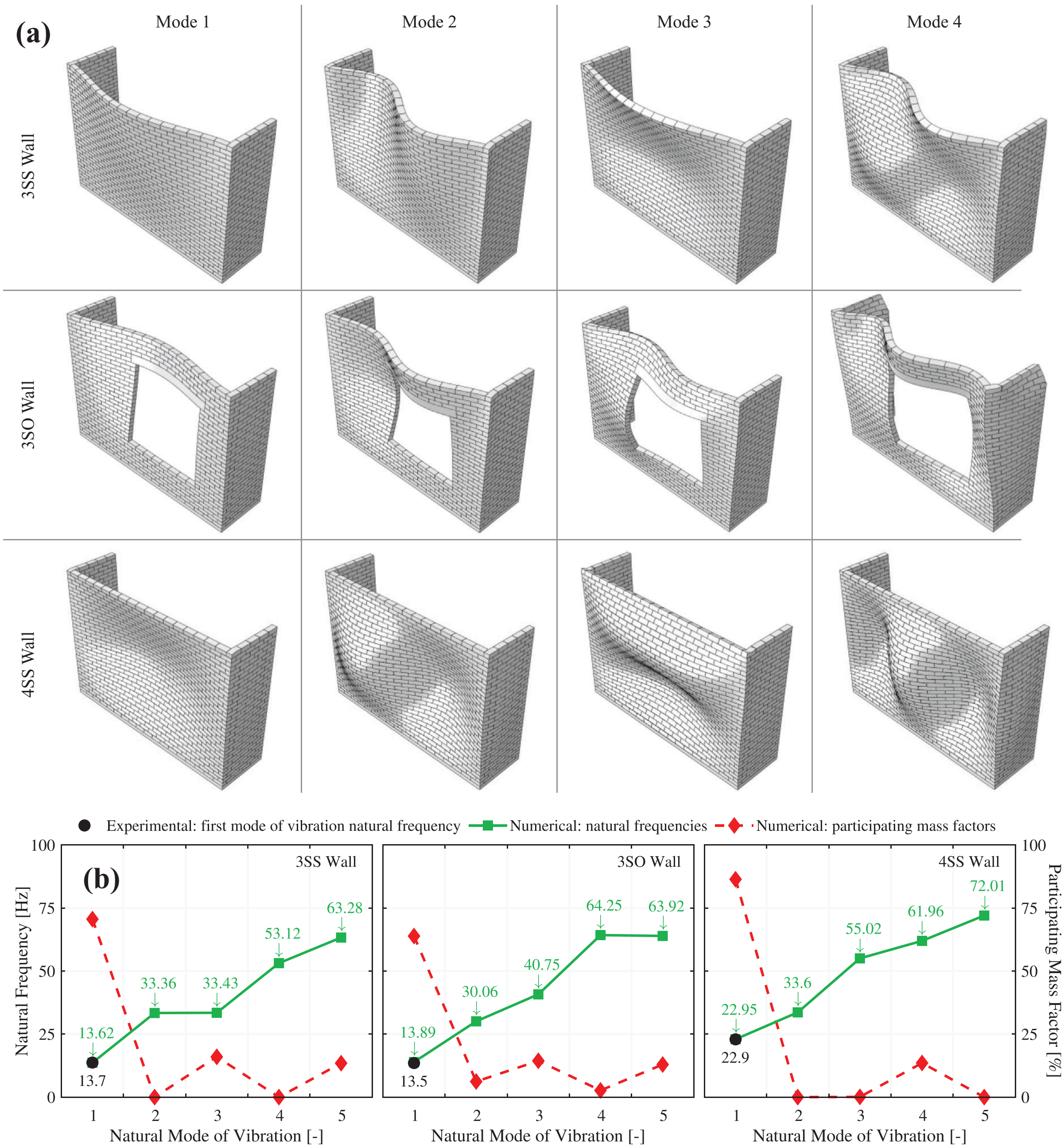


**FIGURE 6** | Results of the modal analysis of the numerical models under self-weight load: modal shapes (a) and natural frequencies and participating mass factors (b).

performance of lower and higher damping ratios is investigated in Section 5. Natural frequency analysis of each numerical specimen is performed preliminarily to assess the effectiveness of the adopted numerical boundary conditions and the elastic material properties to reproduce the experimentally measured fundamental mode of vibration of the walls. The outcomes are also used to calibrate the Rayleigh damping parameters of the numerical models. The modal shape and natural modes of vibration, as well as participating mass factors of the first four natural modes of vibration for each numerical specimen, are shown in Figure 6, along with the first-mode natural frequencies of the pristine experimental specimens obtained from random noise excitation. A good agreement between the numerical and experimental fundamental frequency has been observed for all specimens, with the highest difference being 2.9% in the 3SO specimen. Most of the participating mass of each specimen (more than 70%) is related to the first-to-third natural modes. Hence, the frequencies of the first and third natural modes of vibration are used to calibrate the Rayleigh damping parameters of each wall.

## 4 | Simulation Results

This section provides the outcomes of the simulation of the three benchmark walls, detailing failure mechanisms and crack patterns, displacement and acceleration outputs, hysteretic force-displacement response, and changes in frequency due to damage evolution. The simulation results for the 3SS, 3SO, and 4SS walls are shown in Figures 7, 8, and 9, respectively. These results are first compared against the reference experimental

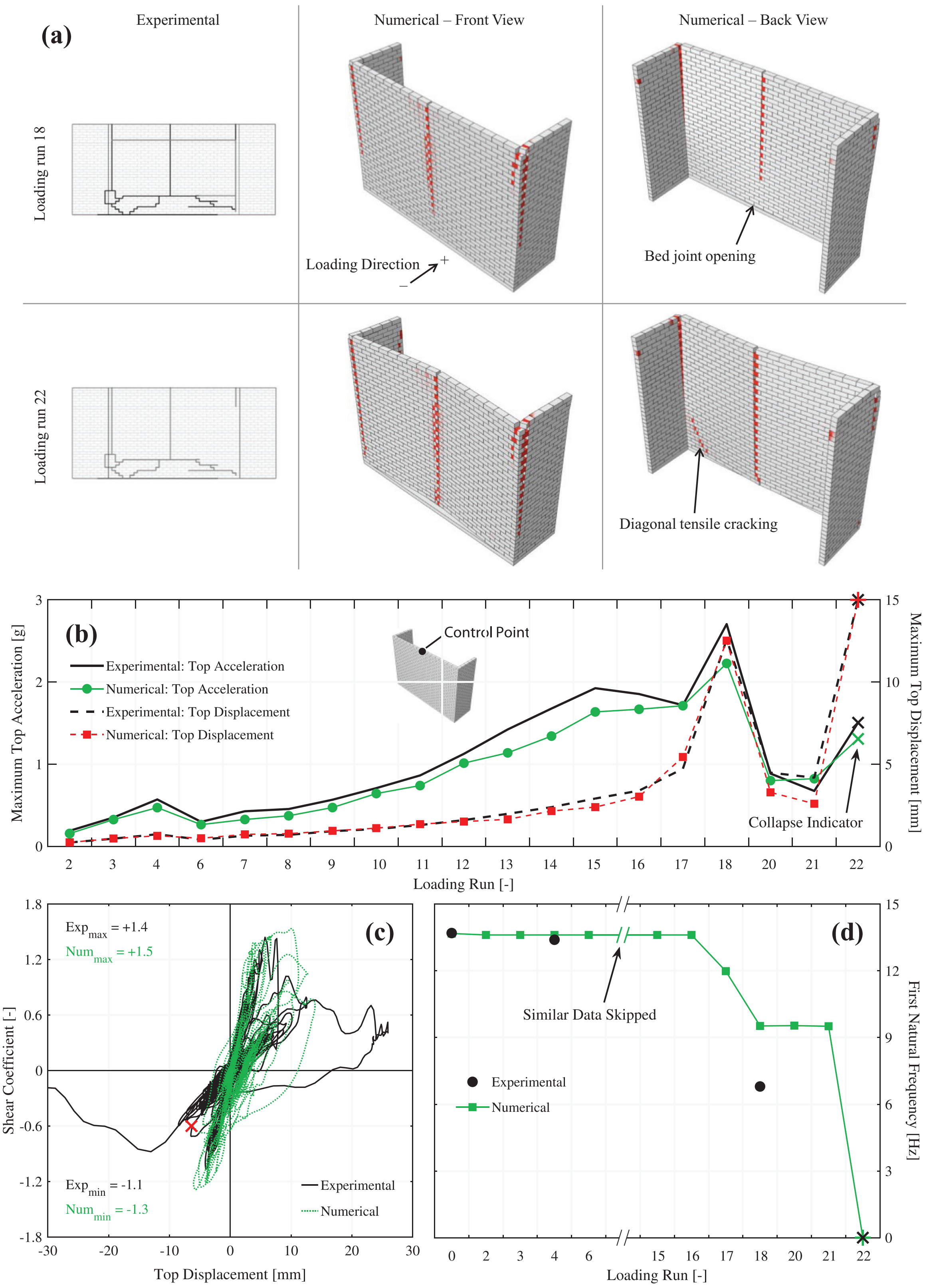


**FIGURE 7** | Simulation results for the 3SS wall: magnified deformed shapes at select loading runs (a), maximum acceleration and displacements recorded at the control point during each loading run (b), hysteretic force-displacement response (c), and evolution of the frequency of the first mode of vibration after each loading run (d).

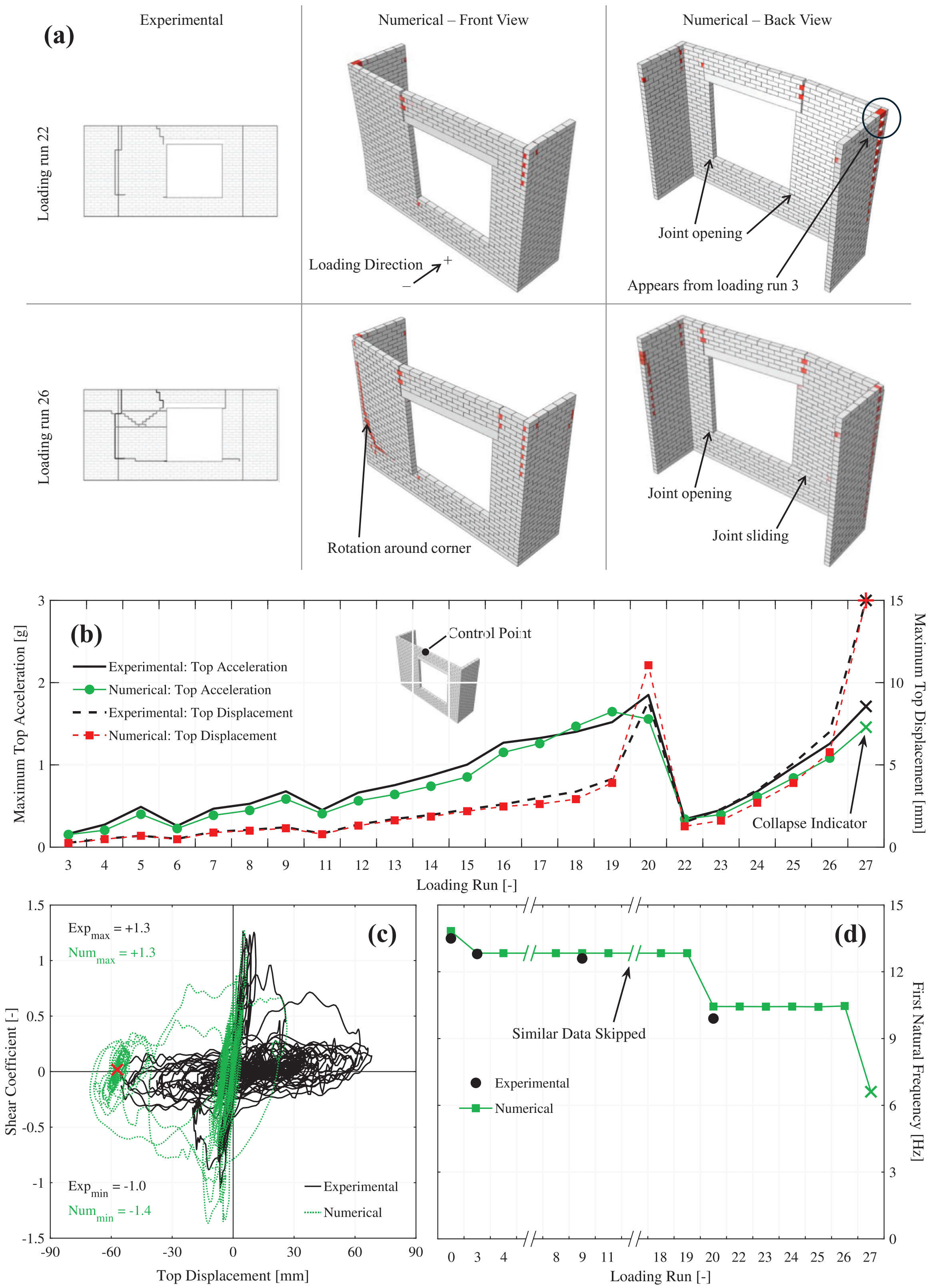


**FIGURE 8** | Simulation results for the 3SO wall: magnified deformed shapes at select loading runs (a), maximum acceleration and displacements recorded at the control point during each loading run (b), hysteretic force-displacement response (c), and evolution of the frequency of the first mode of vibration after each loading run (d).

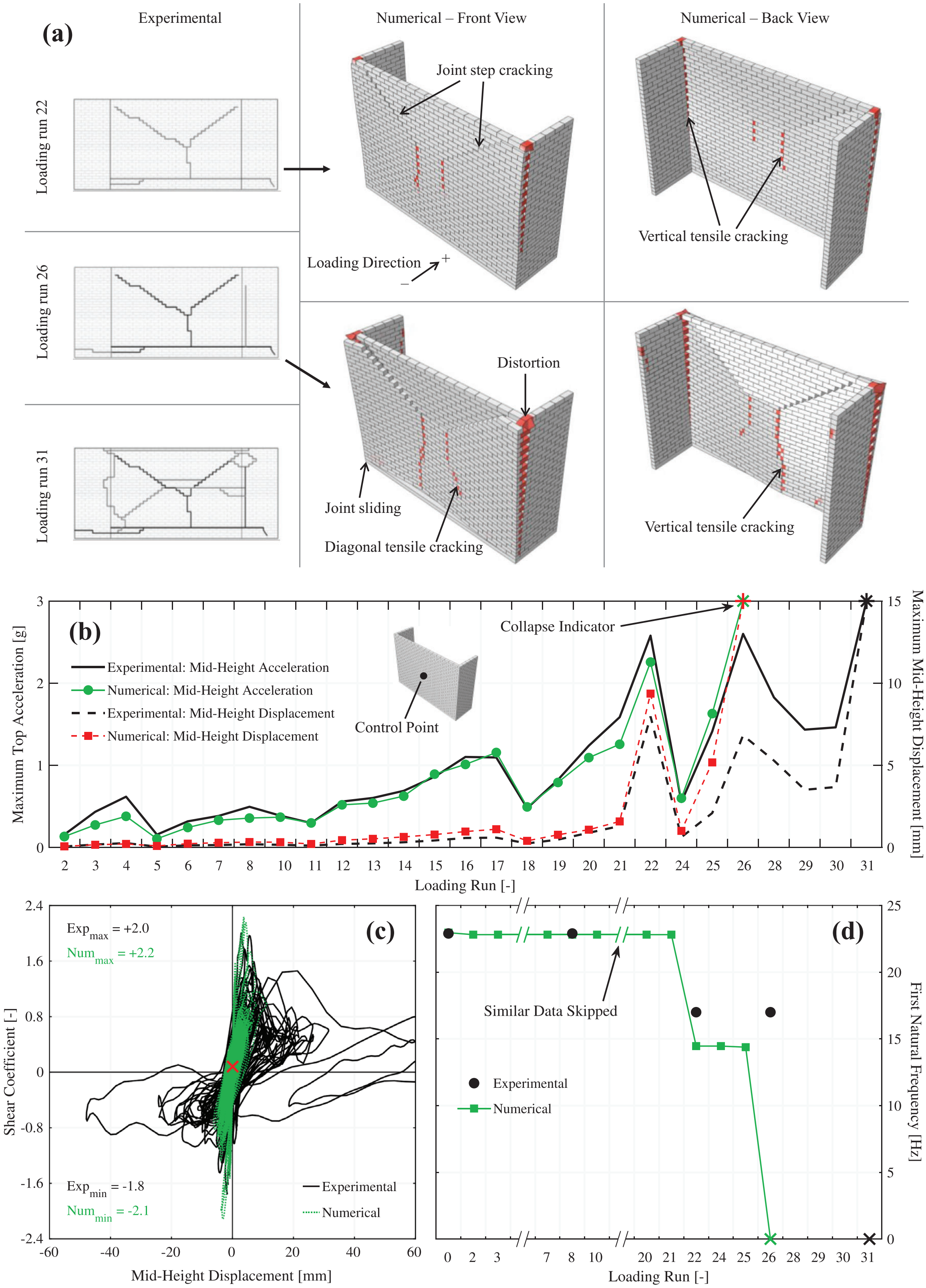


**FIGURE 9** | Simulation results for the 4SS wall: magnified deformed shapes at select loading runs (a), maximum acceleration and displacements recorded at the control point during each loading run (b), hysteretic force-displacement response (c), and evolution of the frequency of the first mode of vibration after each loading run (d).

data to demonstrate the performance of the numerical modeling approach, followed by a discussion on their discrepancies as well as the complexities in simulating each wall.

### 4.1 | Numerical versus Experimental: Performance of the Modeling Strategy

The numerical deformed shapes of the walls during dynamic runs are shown in Figures 7a, 8a, and 9a, compared with the experimental crack propagation maps. Each image captures the moment of maximum deformation at loading runs when new damage appears in the experimental specimens. The regions highlighted in red indicate damage in the blocks all occurred in tension. The primary crack patterns contributing to the wall collapse are also highlighted using arrows and text descriptors. The numerical model demonstrates high accuracy in replicating the primary failure mechanisms observed in the experiments across all specimens, on par with the simulations of [15], closely matching major crack locations and damage progression. For the 3SS wall (Figure 7a), the numerical simulation aligns well with the development of vertical cracks (line failure) at the mid-length of the wall and at the wall-flange connections during loading run 18, as well as the horizontal crack at the wall base during loading run 22. The 3SO specimen (Figure 8a) shows a similar level of resemblance. The vertical cracks at the left wall-flange connection and the top left corner of the window opening during loading run 20 are accurately depicted. The model also replicates the OOP motion of the left (long) pier and the cracks at the right (short) pier during loading run 26. For the 4SS wall (Figure 9a), the model captures the general crack pattern, including vertical cracks at wall-flange connections and stepped and horizontal cracks in the lower wall region. Despite minor differences in the cracking sequence, especially in the 4SS wall, the numerical strategy effectively models both brittle behaviors, like unit splitting in the 3SS wall, and more ductile responses in the 3SO and 4SS walls, where stepped cracks and joint shearing contribute to the failure. The latter shows the reliability of the model in capturing the propagation of discrete cracking of the joints to the smeared continua of the blocks during line failures without the need for alternative measures such as putting discrete potential crack joints in the middle of the blocks as done in previous block-based approaches [46, 67].

The quantitative results of the numerical simulations are summarized in the envelope curves in Figures 7b, 8b, and 9b, comparing the maximum acceleration and displacement experienced at the control point of each wall during different loading runs to the experimental readings. For the 3SS and 3SO walls, the control point is at the top mid-length of the main panel, and for the 4SS wall, it is the mid-height central point of the main panel, as specified in the experimental study [11]. Solid lines represent acceleration data, and dashed lines indicate displacement data, with black lines for experimental and colored lines for numerical readings. The specimens' collapse is marked with a cross (×) for both experiments and numerical simulations. In the displacement curves of the 3SO wall where the experimental and numerical collapse points coincide, the numerical collapse mark is replaced with a plus (+) for clearer highlighting. It should be noted that the collapse in the numerical models is identified as the moment wherein the complete failure mechanism is developed and the end of the loading sequence is reached (3SS and 3SO walls), or the high mechanical and geometrical nonlinearities prevent the numerical convergence in the implicit solver (4SS wall). A strong agreement between experimental and numerical results is seen across all walls, indicating an accurate prediction of deformation demands, inertial effects, and collapse onset. Although the 4SS wall (Figure 9b) numerically collapses during loading run 26 compared to run 31 in the experiment, peak base acceleration values for runs 26 and 13 (1.39 and 1.42 g, respectively) are comparable, as shown in Table 1. This suggests that, despite the difference in collapse run, the model reliably predicts failure at similar intensities, affirming its robustness without any need for recalibration. Moreover, the model compares well with the outcomes of [15] simulating the same walls, showing a more accurate match of the loading runs and intensities corresponding to the initiation and full development of failure mechanisms.

The hysteretic force-displacement responses are shown in Figures 7c, 8c, and 9c, with solid black lines for experimental data and colored curves for numerical results. The numerical forces are normalized by the gravitational weight of the entire geometry to facilitate their comparison with the experimental shear coefficients detailed in [11]. The model effectively captures key response characteristics, including stiffness, peak shear coefficients, and displacements, closely matching the experimental data. Moreover, the numerical hysteretic responses provide an even more accurate approximation of the initial stiffness and near-collapse energy dissipation compared to the previous work in [15]. Two main differences are noted. First, the numerical models show a higher maximum shear coefficient in the negative direction, up to 30% in the 3SO wall, potentially due to over-constraint against backward motion from ideal boundary conditions as well as the effect of flanges, as cited in [25]. Second, in the final experimental cycle, where large displacements are observed, the 3SS numerical model displays lower displacements, and the 3SO wall shows inconsistent energy dissipation compared to the experiment. These differences can be attributed to the inherent unpredictability of collapse dynamics, where minor variations significantly affect the progression. Differences in motion and failure mechanism in the left pier may also explain this discrepancy in the 3SO wall. Additionally, the lower energy dissipation of the 4SS numerical models is attributed to the early collapse of the specimen and the unavailability of the response beyond loading run 26.

Figures 7d, 8d, and 9d illustrate the evolution of the first-mode frequency in the numerical walls as the loading sequence progresses, with line plots for numerical results and dots for experimental random noise runs. Each point reflects the frequency extracted after the complete application of each loading run. The data corresponding to runs where no frequency changes occur are skipped (indicated in the figures with "/ /"). The numerical frequency changes, decreasing with damage, align closely with the experimental records, demonstrating that the adopted boundary conditions and mechanical properties effectively capture the observed behavior in all three walls. Moreover, together with the recorded acceleration and displacements (Figures 7b, 8b, and 9b), this confirms the ability of the model to replicate the gradual progression of damages across long testing sequences such as those adopted in the reference experiments. Nevertheless, minor discrepancies are observed. First, the 3SS numerical wall shows

39% higher damaged frequency compared to the experimental benchmark after loading run 18, likely due to the incomplete formation of a horizontal crack at the base, which also results in a slightly larger cracked stiffness than that of the experimental counterpart beyond this loading run (see Figures 7c). Second, while damage initiation is reported to occur during loading run 18 of the experiment, the first significant change in the first-mode frequency of the 3SS numerical wall is observed in loading run 17. Likewise, both the numerical and experimental 3SO wall frequencies display a sudden reduction at the beginning of the loading sequence. While no damage is reported in the experiment, the 3SO numerical model indicates minor cracks at the intersection of the left flange and larger pier as early as loading run 3. These observations denote the possibility that minor damage, undetectable by visual inspection, could have already occurred in these loading runs of the corresponding tests.

### 4.2 | Complexities Associated with the Simulations

Despite the effectiveness of the model, some discrepancies between numerical and experimental results are observed, mainly due to idealized assumptions in the numerical setup. In the 3SS wall, the model does not capture certain minor crack patterns, such as the horizontal lower crack and stepped cracks in the lower wall region. These discrepancies likely result from the imperfections present in experimental settings not reflected in the numerical model, such as geometrical inconsistencies due to workmanship and spatial variations in material properties. Idealizations such as having perfect block shapes, complete joint connections across all blocks, assuming head joints as strong as bed joints, and uniform material distribution across the geometry regularize the stress distribution and minimize localized stress concentrations, preventing some experimental crack patterns from forming. Additionally, a vertical opening at the right wall-flange connection appears within the flange in the numerical model, while in the experiment, it forms in the main wall. This results from the standardized block layout in the numerical model, which shifts the mid-length crack position and causes stress concentration at the flange/corner interface rather than at the wall/corner intersection. Nonetheless, both numerical and experimental corner cracks indicate similar fracture mechanisms driven by relative bending of the main wall with respect to the flange.

In the 3SO wall, the numerical model does not fully replicate the detachment of the left pier from the flange and its one-way bending motion observed in the experiment. This limitation may stem from model constraints: the blocks' residual tensile strength, retained to prevent numerical divergence, may have prevented the complete separation, causing the pier to rotate around the vertical axis of the wall-flange connection rather than exhibiting one-way bending. Additionally, unaccounted in-plane deformations during the experiment may have also contributed to the mid-height and the stepped cracking of the left pier, which is absent in the numerical model. Another possibility is that the presence of openings may lead to high stress concentrations at the corners that result in the idealized failure mechanism achieved here and in [15] while preventing secondary damages (such as the stepped cracks) specific to the experimental conditions. The numerical model also does not show the horizontal crack extending into the left flange, possibly due to more restrictive boundary conditions in the $x$-direction at the top of the experimental flanges compared to the model, a discrepancy further examined in the sensitivity studies of Section 5. Finally, the lower energy dissipation observed in the hysteretic response of the 3SS and 3SO numerical models may result from overdamping, especially in later loading cycles where frequency changes during collapse cause Rayleigh damping to restrict the rigid-body motions associated with the failure mechanisms of the walls.

The 4SS wall displays differences in cracking sequence and damage patterns between the numerical and experimental results. In the numerical model, the vertical crack at the right wall-flange connection develops earlier (run 22) than in the experiment (run 26), likely due to restrictive numerical boundary conditions that prevent movement or rotation at the wall-flange intersection. In the experiment, such deformations could be absorbed by minor rotations or translations at the back supports, which distributed stress more evenly across the structure. The idealized numerical boundary conditions restrict this flexibility, leading to early vertical cracking and detachment of the wall from the flanges. Additionally, the horizontal crack at the wall base opens partially at loading run 22 and fully by run 26 in the model, while in the experiment, it appears more prominently at run 22, forming four courses above the base. The delay in base crack formation and the replacement of the stepped crack observed in the experimental lower-right region with a diagonal crack in the numerical model may result from adopting material properties based on the average of experimentally reported small-scale behaviors. Moreover, the model idealizations encourage cracks to form at maximum flexure points, such as the wall base. The excessive distortions at the top corners of the numerical 4SS wall are attributed to the coupling conditions between the top of the corner blocks and the main wall reference point. In the experiment, clamping profiles attached to the top beam and the sides of the corner bricks confined these areas, effectively limiting deformation. In contrast, the coupling setup in the numerical model allows more flexibility, leading to distortions not observed experimentally. Section 5 further explains that this coupling is essential for activating the failure mechanism and damage progression in the numerical 4SS wall.

Finally, the mid-height horizontal crack at the right side of the main experimental panel is absent in the 4SS model, and the right half of the numerical panel shows a different one-way bending deformation. These, along with the earlier collapse (run 26 instead of 31) of the 4SS numerical model, can be attributed to variations in input motions. Even though filtering is needed for accuracy, certain low- and high-frequency components may be lost during the noise-reduction process, particularly affecting the artificial SSW signal, which covers all frequency ranges. The filtering process significantly impacts base displacements while maintaining consistent acceleration data. Figure 10 illustrates this effect on the base motion in loading run 26, where double-integrated filtered base acceleration data produced peak negative displacements and low-frequency oscillations not observed in the direct experimental readings, likely contributing to the early collapse of the model. This discrepancy underscores the importance of using input motions closely aligned with the actual

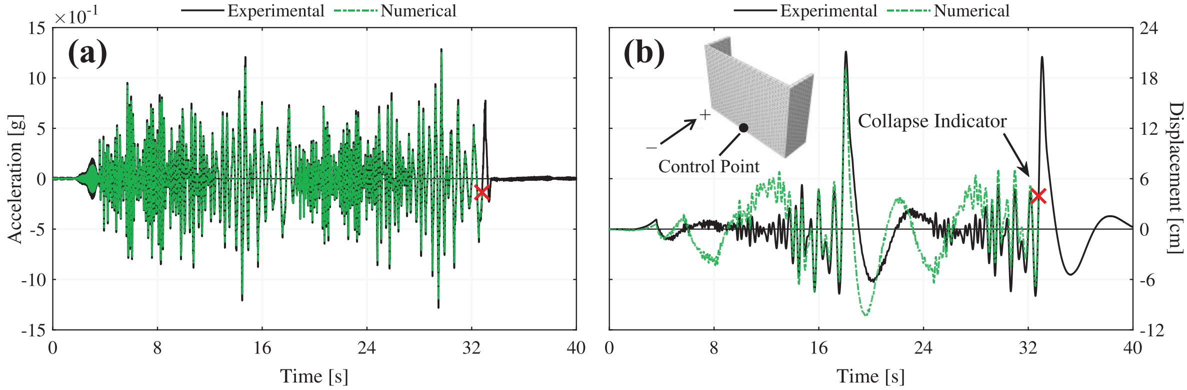


**FIGURE 10** | Comparison of experimental and numerical base motions in loading run 26 of the 4SS wall: input acceleration time histories (a) resultant base displacements (b).

experimental environment, as even minor deviations in applied motions can alter dynamic responses.

## 5 | Sensitivity Study of The Variability of Dynamic Behaviors

The results presented in Section 4 demonstrate the potential to extend the modeling strategy proposed in [49] for reliably modeling the two-way bending OOP dynamic behavior of URM masonry walls. Moreover, the calibrated numerical models make possible the study of the influence of different parameters such as material properties, damping ratio, loading direction, and boundary conditions on the dynamic behavior of the benchmark specimens. The sensitivity study discussed in this section is performed to investigate these effects further. These results should be regarded as representations of alternative behaviors that could have emerged during the experiments, given the uncertainties associated with the testing conditions and the chaotic nature of dynamic behavior.

### 5.1 | Reduction of Computational Efforts

Before conducting the sensitivity study, efforts are made to reduce computational demand. Each of the high-fidelity simulations presented in Section 4 takes an average of 550 h on moderately powerful hardware (16 CPU cores @4.2 GHz clock speed) when the complete loading sequences are considered. This presents a bottleneck and a major hindrance to generating new understanding of the dynamic OOP responses by simulating cases that are not studied experimentally. Hence, similar to [49], the information regarding damage initiation and propagation is used to simplify the loading sequence independently for each numerical wall. It was found that removing the low-amplitude loading runs from the numerical loading sequence and initiating the analyses from the first run with a noticeable influence on frequency changes (run 17 in the 3SS wall, run 20 in the 3SO wall, and run 22 in the 4SS wall) can significantly reduce the average computational time to 230 h on the same hardware. This, being a 60% improvement compared to the original full-sequence simulations, does not alter the response of the numerical specimens in any manner. In fact, the simplified simulations of all three walls show the exact same response as the original analyses in terms of collapse onset, failure mechanism, and quantitative response discussed in Section 4. Hence, the models with simplified loading sequences of Table 3 (simply referred to as "simplified" models) are used to analyze the variations reported in this section. It should be noted that in the 4SS wall, the simplified simulations are carried out under the 0.05 MPa vertical compression used in the experiment for the considered runs.

### 5.2 | Numerical Model Variations

Table 4 lists the different parameters considered for each variation, with the parameters deviating from the original simulations highlighted in bold. It should be noted that in each variation, only one parameter is changed while the others remain at their original values. Each variation is identified as Vi, with "i" denoting the number of the variation, being V0, the original numerical models subjected to the simplified loading sequence. The variations V1 to V3 are conceived to check the influence of boundary conditions, specifically those considered for the top of the flanges. In V1, the top of the flanges is fixed also in the $x$-direction. V2 models maintain the original constraints but extend the coupling area to half the length of the corner bricks. For the 4SS wall, V2 variations require uncoupling half the corner brick surfaces from the main-top reference point; thus, V3 is included as an intermediate variation where only the coupling of the corner block half-surfaces is removed. The V4 variations simulate a scenario with reversed loading direction, meaning that the sign of all input signals in Table 3 is reversed. Figure 11 further clarifies the boundary conditions and loading directions across V0 to V4 models. Variations V5 and V6 explore the impact of material properties, specifically the tensile strength of the zero-thickness joints ($f_t$). V5 models use a 0.01 MPa lower $f_t$, and V6 variations are modeled with 0.01 MPa higher $f_t$ compared to the reference models, resulting in an 8.3% variation of the parameter, which is well below the 31% coefficient of variation reported in material-level experiments [11] and a very minor variation. Finally, the sensitivity of response to the amount of Rayleigh damping is investigated in V7 and V8 variations where lower and higher target damping ratios ($\zeta_R$ =3% and 8%) are considered, respectively. The 3% damping ratio is adopted as the lowest value deemed appropriate during the investigation of one-way bending dynamic OOP behaviors [49]. The 8% ratio is adopted to include an extreme case of the overdamped response.

**TABLE 3** | Simplified loading sequence adopted in the sensitivity study.

| 3SS wall | | | | 3SO wall | | | | 4SS wall | | | |
|---|---|---|---|---|---|---|---|---|---|---|---|
| Run # | Input | Scale | PTA* [g] | Run # | Input | Scale | PTA* [g] | Run # | Input | Scale | PTA* [g] |
| 0.05 MPa vertical compression (flanges) | | | | 0.05 MPa vertical compression (flanges) | | | | 0.05 MPa vertical compression (entire wall) | | | |
| 17 | FEQ2-DS4 | 350% | −1.10 | 20 | FEQ2-DS4 | 400% | −1.28 | 22 | FEQ2-DS4 | 600% | −1.93 |
| 18 | FEQ2-DS4 | 400% | −1.28 | 22 | FHUIZ-DS0 | 100% | −0.15 | 24 | SSW×2 | 75% | +0.38 |
| 20 | FHUIZ-DS0 | 100% | −0.15 | 23 | FEQ2-DS3 | 100% | −0.25 | 25 | SSW×2 | 200% | +0.99 |
| 21 | FEQ2-DS3 | 100% | −0.24 | 24 | FEQ2-DS4 | 100% | −0.33 | 26 | SSW×2 | 250% | +1.39 |
| 22 | FEQ2-DS4 | 100% | −0.62 | 25 | FEQ2-DS4 | 150% | −0.46 | 28 | SSW×2 | 150% | +0.92 |
| | | | | 26 | FEQ2-DS4 | 200% | −0.78 | 29 | SSW×2 | 150% | +0.81 |
| | | | | 27 | FEQ2-DS4 | 300% | −0.91 | 30 | SSW×2 | 150% | +0.66 |
| | | | | | | | | 31 | SSW | 100% | +1.42 |

*Recorded peak table acceleration.

**TABLE 4** | Different numerical variations considered for the sensitivity study.

| | Coupling* | | Boundary constraints | Loading | Material | Damping |
|---|---|---|---|---|---|---|
| Variation | Flange-top | Main-top** | Flange-Top *X*-Translation | Direction | Joints $f_t$ | $\zeta_R$ |
| V0 | Original | Original | Free | Original | 0.12 MPa | 5% |
| V1 | Original | Original | **Fixed** | Original | 0.12 MPa | 5% |
| V2 | **Extended** | **Main panel** | Free | Original | 0.12 MPa | 5% |
| V3** | Original | **Main panel** | Free | Original | 0.12 MPa | 5% |
| V4 | Original | Original | Free | **Reversed** | 0.12 MPa | 5% |
| V5 | Original | Original | Free | Original | **0.11 MPa** | 5% |
| V6 | Original | Original | Free | Original | **0.13 MPa** | 5% |
| V7 | Original | Original | Free | Original | 0.12 MPa | **3%** |
| V8 | Original | Original | Free | Original | 0.12 MPa | **8%** |

*Different couplings are depicted in Figure 11.
**Only for the 4SS wall.
*Note:* The parameters deviating from the original simulations are highlighted in bold.

### 5.3 | Analysis Outcomes

The outcomes of the sensitivity study are presented herein. Table 5 provides an overview of the collapse run for each variation, categorized into three groups: "Reference Collapse," where collapse occurs at the same loading run as the original models; "Early Collapse," where collapse occurs at earlier runs; "No Collapse," where stability is maintained until the end of the simulation, with either no damage or incomplete failure mechanisms. The final deformed shapes are classified into four different types based on the development of the failure mechanism and are illustrated in Figure 12. They consist of a "Reference Mechanism" type wherein the failure patterns are similar to those of the original numerical models, an "Incomplete Mechanism" type where only parts of the original crack patterns are obtained by the end of the analysis, a "Severe Mechanism" type with cracks even more pronounced compared to the original models, and a "No Mechanism" type where the specimens show from no to very minor damages. In this last category, not only is the original mechanism recreated, but additional damage is also observed. The maximum accelerations and displacements experienced at the control points of the numerical variations at different runs are shown in Figure 13.

### 5.4 | Implications for the Study of Dynamics in URM Walls

The behavior of different variations of each wall is compared herein based on their final deformed shape and collapse status. The role of boundary conditions is explored by comparing variations V1 to V3 with the reference model V0. Fixing the translational DoF for the flange-top reference points does not significantly affect the 3SS and 3SO walls. The V1 variations of both walls, when compared to V0 specimens, collapse at the same loading runs and show similar failure mechanisms, with only the vertical crack at the top right corner of the window in the 3SO wall being replaced by a diagonal step crack extending to the corner of

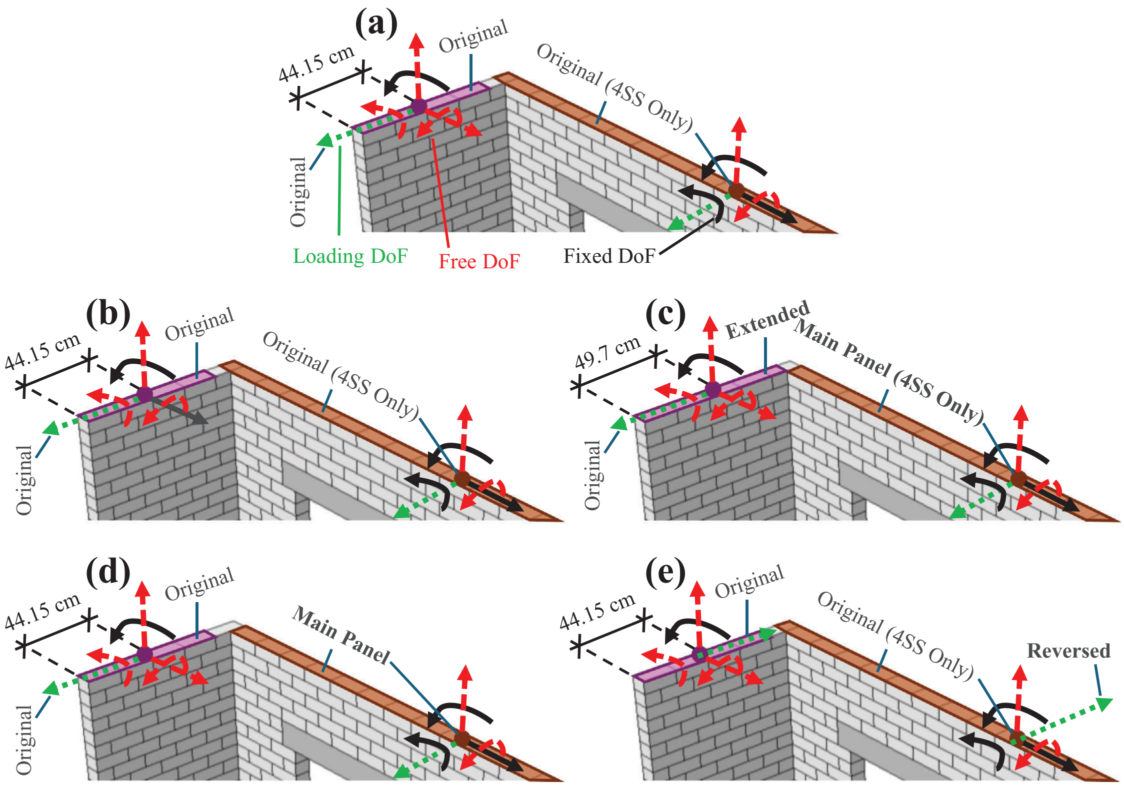


**FIGURE 11** | Boundary and loading variations considered in the parametric study: V0 (a), V1 with fixed flange-top *x*-translations (b), V2 with extended flange-top couplings (c), V3 with released corner couplings (d), and V4 with reversed loading direction (e).

**TABLE 5** | The final loading run and overall outcome corresponding to different variations of the sensitivity study.

| Variation | 3SS wall | | 3SO wall | | 4SS wall | |
|---|---|---|---|---|---|---|
| | **Final run** | **Outcome (Mechanism*)** | **Final run** | **Outcome (Mechanism)** | **Final run** | **Outcome (Mechanism)** |
| V0 | 22 | Reference collapse (a) | 27 | Reference collapse (a) | 26 | Reference collapse (a) |
| V1 | 22 | Reference collapse (a) | 27 | Reference collapse (a) | 26 | No collapse (b) |
| V2 | 18 | Early collapse (c) | 20 | Early collapse (a) | 31 | No collapse (d) |
| V3** | — | — | — | — | 31 | No collapse (b) |
| V4 | 22 | No collapse (d) | 27 | No collapse (c) | 31 | No collapse (d) |
| V5 | 18 | Early collapse (c) | 20 | Early collapse (a) | 22 | Early collapse (c) |
| V6 | 22 | No collapse (b) | 27 | No collapse (d) | 31 | No collapse (d) |
| V7 | 22 | No collapse (b) | 27 | No collapse (d) | 31 | No collapse (d) |
| V8 | 17 | Early collapse (c) | 20 | Early collapse (c) | 22 | Early collapse (c) |

*Parentheses indicate the deformed shape observed at the end of the analysis, shown in Figure 12.
**Only for the 4SS wall.

the wall. The 4SS wall, on the other hand, is noticeably affected by the new boundary conditions. Although the wall collapses during loading run 26, similar to the V0 specimen, it shows a premature failure mechanism without the bed joint crack at the base and the vertical tensile cracks at the center of the wall. The high sensitivity of the dynamic simulations to the boundary conditions is further revealed by the V2 variations, where the slight extension of the flange-top coupling area leads to the early collapse of both 3SS and 3SO walls and, on the other hand, prevents the collapse of the 4SS wall entirely. Moreover, the V3 variation of the 4SS wall does not reach collapse conditions either.

The V4 variations, analyzed under reversed-direction loading motions, exhibit entirely different deformation patterns than the reference models. Instead of the horizontal bending observed in the V0 model, the 3SS wall shows a vertical bending motion where

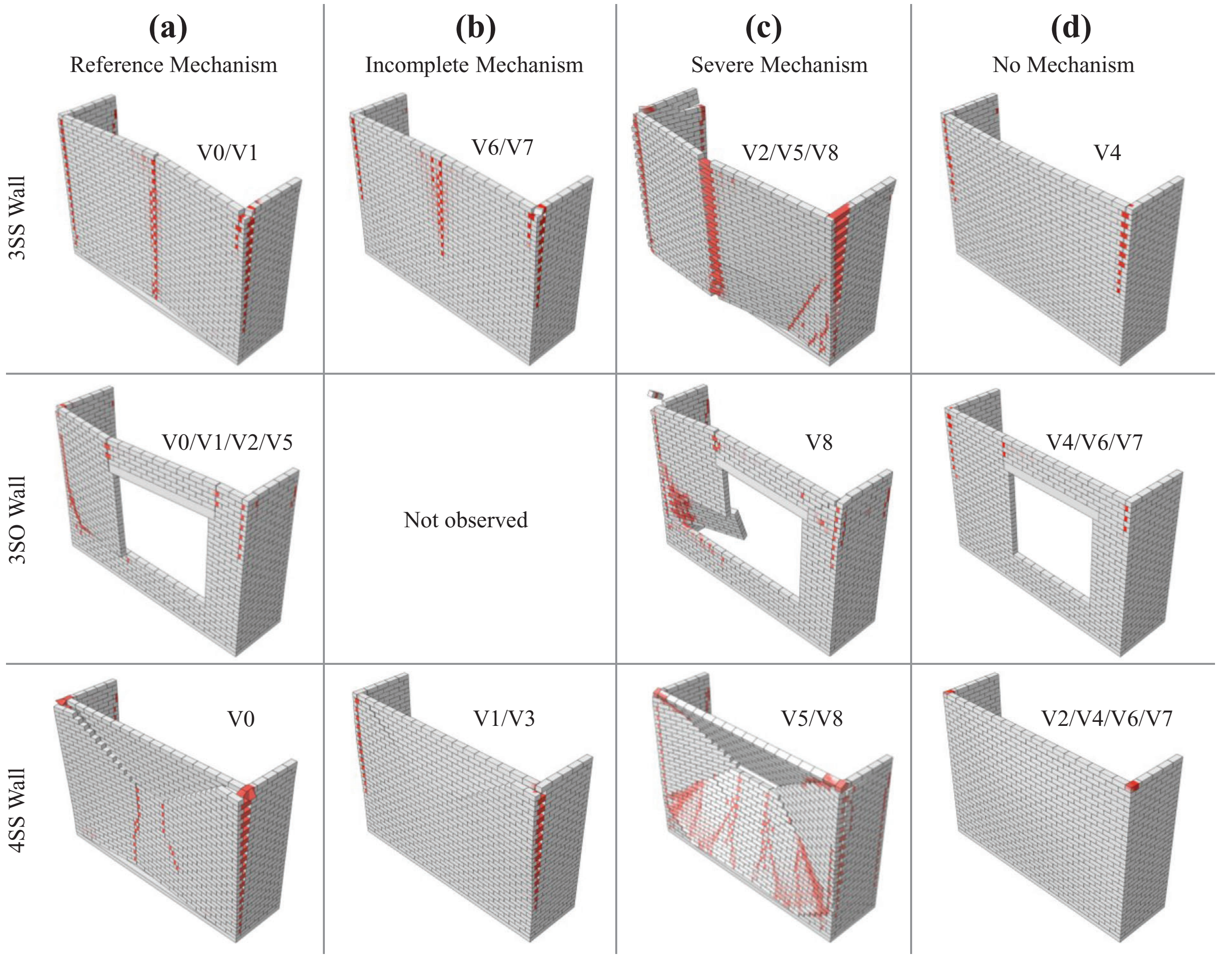


**FIGURE 12** | Typical final deformed shapes observed across different simulations of the sensitivity study: when regular (a), incomplete (b), or severe (c) failure mechanism is formed, and when no mechanism is obtained (d).

damages are solely concentrated at the wall-flange connections in the form of vertical Mode-II shear cracks. The 3SO wall shows a similar change where the damage is mainly caused by the horizontal bending at the top of the left (long) pier and the spandrel at the top of the wall. None of the three V1 walls collapse by the end of the simulation. No visible damage appears in the deformed shape of the 4SS wall. This suggests that the assumption of the loading direction is crucial due to the asymmetric position of the return walls.

As expected, the performance of V5 and V6 variations highlights the remarkable sensitivity of the performance of the numerical simulations to the adopted material properties. It should be noted that the aim of these variations has not been to comprehensively quantify the sensitivity to material properties in a manner that could be generalized to other cases. For instance, the behavioral variations observed can also be dependent on the specific material properties of the walls under study, as specimens with stronger units may have shown different sensitivities compared to the weak-unit ones studied here. Nevertheless, it is interesting to see that this effect is of high importance for dynamic analyses where many known and unknown factors contribute to the behavior of the models. A 0.01 MPa reduction of the tensile strength in the joints leads to an early collapse in all three V5 walls upon reaching their first high-intensity loading run. Interestingly, the V5 simulation of the 4SS wall shows the complete failure mechanism observed in the experiment since diagonal cracks at the lower portion of the wall have been able to form. On the other hand, an increase in the tensile strength with the same magnitude can prevent (partially or completely) the collapse of the walls. It is also observed in the V6 walls that damage is concentrated in the blocks since the joints previously opened in the V0 models have a higher strength. The findings here imply that a deterministic approach to dynamic simulation of such complex experiments leads to a partial understanding of the dynamic response and should not be adopted. Moreover, one should also consider the spatial variation of the material properties in the wall, as well as the differences between bed and head joints. Finally, the extent of sensitivity to material properties may vary when different modeling approaches, for instance distinct element [15] or applied element [68] methods with rigid blocks, are adopted.

The V7 variation shows a stronger behavior when using 3% damping, while V8 walls with 8% damping collapse during the very first loading run. A similar effect has been observed when studying the one-way bending dynamic behaviors in [49]. This differing behavior arises from assumptions in the Rayleigh damping approach, where input parameters are set with equal target damping ratios for specific wall modal frequencies. This results in underdamping (below target $\zeta_R$) within the frequency

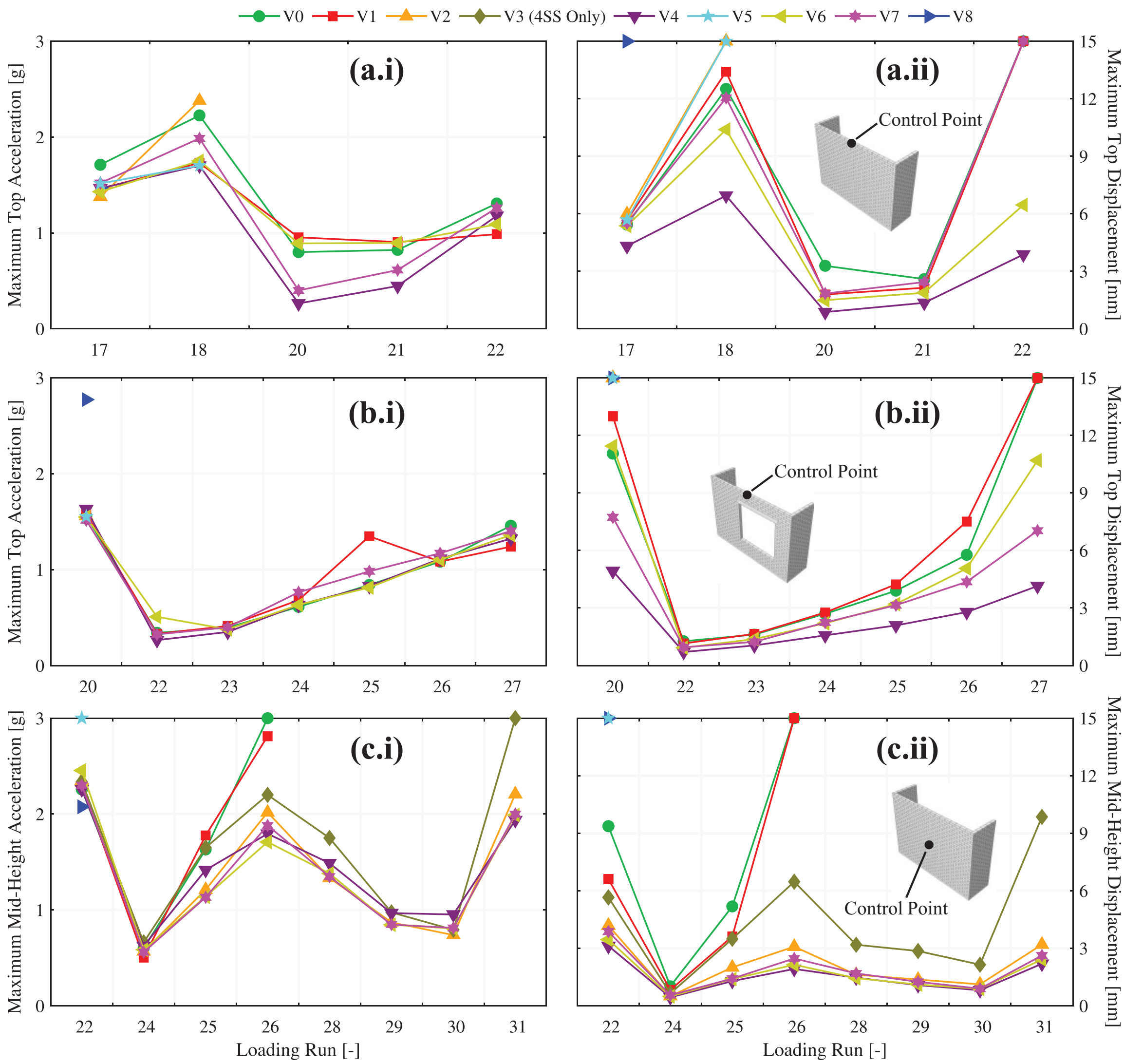


**FIGURE 13** | Accelerations and displacements of the numerical variations considered in the sensitivity study: maximum accelerations (i) and displacements (ii) recorded at the control points of the 3SS (a), 3SO (b), and 4SS (c) walls during different loading runs.

range and overdamping (above $\zeta_R$) outside it. Low $\zeta_R$ values fail to dissipate sufficient energy across all frequencies, while high $\zeta_R$ values overdamp the response, emphasizing the deformation mode with the largest participating mass and leading to rapid collapse. An appropriate damping ratio, ideally between 2% and 5% [69], is crucial for accurate response. However, due to dynamic variability, even moderate values like 3% in V7 may still yield different results than the expected ones. Overall, this study identifies V0 models as the most representative of benchmark experiments and suggests a 5% damping ratio as an effective initial estimate. It should be noted that part of the sensitivity to damping can be affected by the choice of the solver type. For instance, numerical procedures using an explicit solver may show different variability of the results when damping is changed.

Aside from differences in collapse behaviors and failure patterns, the small variations considered in this study also produce different acceleration and displacement outputs. Figure 13 shows that maximum acceleration data are less sensitive to variations if compared to the maximum displacement data. Even displacement demands show large scatters only in high-intensity loading runs—specifically, loading runs 18 and 22 in 3SS, 20 and 22 in 3SO, and 18, 26, and 31 in 4SS. In these cases, the effects of the adopted variations are only activated when the specimens approach collapse conditions, where the dynamic responses are more chaotic. It should be noted that given the complexity and sensitivity of the model to numerous parameters, such as damping values and material properties, other combinations of these (not explored herein) may have also yielded satisfactory results. Therefore, adopting a systematic calibration procedure, such as the one in this study, is key to preventing the process from becoming interminable. Hence, it is recommended to conduct modeling by setting up the geometry and the boundary conditions, followed by selecting an appropriate damping ratio, and finally prescribing the material properties.

## 6 | Conclusions

This study proposes a computational modeling strategy for the detailed study of the OOP two-way bending behaviors in URM walls. A high-fidelity block-based numerical model, originally proposed in [48] for static analyses and later extended to the dynamic framework in [49], is used for the first time to reproduce several experimental incremental dynamic tests of two-way spanning calcium silicate return walls with different geometries and boundary conditions subjected to long multi-step sequences of shake table loading. Additionally, the study examines the influence of different modeling considerations on the two-way bending dynamic responses. The main findings of this study are as follows:

- The modeling strategy reliably reproduced the response of the benchmark experiments under sequential earthquake loading. The strategy also consistently captured the complex behavior across all three benchmarks despite differences in geometry, with a single set of assumptions for material properties and boundary conditions.
- The implicit solver effectively simulated dynamic behaviors up to collapse. Rayleigh damping in the blocks proved effective in capturing energy dissipation without increasing the computational demands due to its combination with the implicit solver.
- The computational demands can be reduced up to 60% by simplifying the loading sequence of each wall and removing seismic loading runs with no effect on the response of the specimens.
- The importance of the accuracy of input motions was highlighted by the 4SS wall, where slight deviations in applied acceleration data compared to those experienced by the experimental benchmark led to substantial differences in displacements at the wall base and an earlier-than-expected collapse.
- The sensitivity study showed that a careful selection of boundary conditions is crucial to accurately reflect the real-world constraints, though even the best assumptions may not perfectly replicate experimental deformation patterns or failure mechanisms.
- High variability of the results from minor changes in boundary conditions, material properties, and damping ratio underscores the chaotic nature of dynamic behaviors, reinforcing the need for a probabilistic approach to dynamic analysis of these structures. A probabilistic approach to dynamic analyses is also made possible by the numerical strategy proposed in this study.
- A 5% damping ratio resulted in reasonable energy dissipation and peaks in experienced acceleration and displacements.

The numerical modeling procedure presented in this study enables the study of dynamic responses in walls with complex geometrical and boundary conditions, such as gable walls or masonry infills in frame structures, which have been found practically vulnerable in case of earthquakes. The two-way spanning models provide sufficiently reliable benchmarks for the study of dynamic OOP behaviors under various structural conditions, including varying levels of in-plane pre-damage and pre-deformation. Finally, these findings help bridge knowledge gaps in the real-world dynamics of masonry walls and contribute to enhancing the accuracy of more simplified modeling strategies.

## Author Contributions

**Amirhossein Ghezelbash**: conceptualization, methodology, software, validation, formal analysis, investigation, data curation, resources, writing – original draft, writing – review and editing, visualization, funding acquisition. **Satyadhrik Sharma**: conceptualization, methodology, validation, data curation, writing – review and editing, supervision. **Antonio Maria D'Altri**: conceptualization, methodology, software, validation, writing – review and editing, supervision, funding acquisition. **Paulo B. Lourenço**: validation, writing – review and editing, supervision, funding acquisition. **Jan G. Rots**: conceptualization, validation, writing – review and editing, supervision, project administration, funding acquisition. **Francesco Messali**: conceptualization, methodology, validation, resources, data curation, writing – review and editing, supervision, project administration, funding acquisition.


## Acknowledgments

All experimental data used as a benchmark in this study were produced as part of the "Study of the Vulnerability of Masonry Buildings in Groningen" project at the EUCENTRE Foundation, Pavia, Italy. This project was undertaken within the framework of the research program for hazard and risk of induced seismicity in Groningen, sponsored by the Nederlandse Aardolie Maatschappij BV. The authors thank the EUCENTRE Foundation for providing ready access to the data.


## Data Availability Statement

All data and code that support the findings of this study are available from the author upon reasonable request.

## References


1. E. A. W. Hendry, "Masonry Walls: Materials and Construction," *Construction and Building Materials* 15, no. 8 (2001): 323–330, https://doi.org/10.1016/S0950-0618(01)00019-8.

2. L. Moon, D. Dizhur, I. Senaldi, et al., "The Demise of the URM Building Stock in Christchurch During the 2010–2011 Canterbury Earthquake Sequence," *Earthquake Spectra* 30, no. 1 (2014): 253–276, https://doi.org/10.1193/022113EQS044M.

3. A. W. Page, "The Newcastle Earthquake—Behaviour of Masonry Structures," *Masonry International* 5 (1991): 11–18.

4. A. Penna, P. Morandi, M. Rota, C. F. Manzini, F. da Porto, and G. Magenes, "Performance of Masonry Buildings During the Emilia 2012 Earthquake," *Bulletin of Earthquake Engineering* 12, no. 5 (2014): 2255–2273, https://doi.org/10.1007/s10518-013-9496-6.

5. C. Oyarzo-Vera and M. C. Griffith, "The Mw 6.3 Abruzzo (Italy) Earthquake of April 6th, 2009: On Site Observations," *Bulletin of the New Zealand Society for Earthquake Engineering* 42, no. 4 (2009): 302–307.

6. D. F. D'Ayala and S. Paganoni, "Assessment and Analysis of Damage in L'Aquila Historic City Centre After 6th April 2009," *Bulletin of Earthquake Engineering* 9, no. 1 (2011): 81–104, https://doi.org/10.1007/s10518-010-9224-4.

7. T. M. Frankie, B. Gencturk, and A. S. Elnashai, "Simulation-Based Fragility Relationships for Unreinforced Masonry Buildings," *Journal of Structural Engineering* 139, no. 3 (2013): 400–410, https://doi.org/10.1061/(ASCE)ST.1943-541X.0000648.

8. L. Sorrentino, D. D'Ayala, G. de Felice, M. C. Griffith, S. Lagomarsino, and G. Magenes, "Review of Out-of-Plane Seismic Assessment Techniques Applied to Existing Masonry Buildings," *International Journal of Architectural Heritage* (2016): 1–20, https://doi.org/10.1080/15583058.2016.1237586.

9. L. Chang, J. G. Rots, and R. Esposito, "Influence of Aspect Ratio and Pre-Compression on Force Capacity of Unreinforced Masonry Walls

in Out-of-Plane Two-Way Bending," *Engineering Structures* 249 (2021): 113350, https://doi.org/10.1016/j.engstruct.2021.113350.

10. J. Vaculik and M. C. Griffith, "Out-of-plane Shaketable Testing of Unreinforced Masonry Walls in Two-Way Bending," *Bulletin of Earthquake Engineering* 16, no. 7 (2018): 2839–2876.

11. F. Graziotti, U. Tomassetti, S. Sharma, L. Grottoli, and G. Magenes, "Experimental Response of URM Single Leaf and Cavity Walls in Out-of-Plane Two-Way Bending Generated by Seismic Excitation," *Construction and Building Materials* 195 (2019): 650–670, https://doi.org/10.1016/j.conbuildmat.2018.10.076.

12. P. X. Candeias, A. C. Costa, N. Mendes, A. A. Costa, and P. B. Lourenço, "Experimental Assessment of the out-of-Plane Performance of Masonry Buildings through Shaking Table Tests," *International Journal of Architectural Heritage* (2016): 1–28, https://doi.org/10.1080/15583058.2016.1238975.

13. D. Malomo and M. J. DeJong, "A Macro-Distinct Element Model (M-DEM) for Simulating In-Plane/Out-of-Plane Interaction and Combined Failure Mechanisms of Unreinforced Masonry Structures," *Earthquake Engineering & Structural Dynamics* 51, no. 4 (2022): 793–811, https://doi.org/10.1002/eqe.3591.

14. F. Vanin, A. Penna, and K. Beyer, "A Three-Dimensional Macroelement for Modelling the In-Plane and Out-of-Plane Response of Masonry Walls," *Earthquake Engineering & Structural Dynamics* 49, no. 14 (2020): 1365–1387, https://doi.org/10.1002/eqe.3277.

15. D. Malomo, R. Pinho, and A. Penna, "Numerical Modelling of the Out-of-Plane Response of Full-Scale Brick Masonry Prototypes Subjected to Incremental Dynamic Shake-Table Tests," *Engineering Structures* 209 (2020): 110298, https://doi.org/10.1016/j.engstruct.2020.110298.

16. N. A. Nodargi and P. Bisegna, "A Variational-based Non-Smooth Contact Dynamics Approach for the Seismic Analysis of Historical Masonry Structures," *Computer Methods in Applied Mechanics and Engineering* 432 (2024): 117346, https://doi.org/10.1016/j.cma.2024.117346.

17. N. A. Nodargi and P. Bisegna, "A Variational Event-Driven Approach for the Dynamic Analysis of Multi-Block Historical Masonry Structures Under Ground Excitation," *Engineering Structures* 306 (2024): 117804, https://doi.org/10.1016/j.engstruct.2024.117804.

18. F. P. A. Portioli, "Rigid Block Modelling of Historic Masonry Structures Using Mathematical Programming: A Unified Formulation for Non-Linear Time History, Static Pushover and Limit Equilibrium Analysis," *Bulletin of Earthquake Engineering* 18, no. 1 (2020): 211–239, https://doi.org/10.1007/s10518-019-00722-0.

19. V. L. Chong, "The Behaviour of Laterally Loaded Masonry Panels With Openings" (PhD diss., University of Polymouth, 1993).

20. R. Van der Pluijm, "Out-of-Plane Bending of Masonry: Behaviour and Strength" (Phd diss., Technische Universiteit Eindhoven, 1999).

21. C. Liang, "Experimental and Theoretical Investigation of the Behaviour of Brickwork Cladding Panel Subjected to Lateral Loading" (PhD diss., University of Edinburgh, 1996).

22. H. Derakhshan, W. Lucas, P. Visintin, and M. C. Griffith, "Out-of-Plane Strength of Existing Two-Way Spanning Solid and Cavity Unreinforced Masonry Walls," *Structures* 13 (2018): 88–101, https://doi.org/10.1016/j.istruc.2017.11.002.

23. T. T. Bui and A. Limam, "Out-of-Plane Behaviour of Hollow Concrete Block Masonry Walls Unstrengthened and Strengthened With CFRP Composite," *Composites Part B: Engineering* 67 (2014): 527–542, https://doi.org/10.1016/j.compositesb.2014.08.006.

24. F. Messali, G. Ravenshorst, R. Esposito, and J. G Rots, "Large-Scale Testing Program for the Seismic Characterization of Dutch Masonry Walls," paper presented at the 16th World Conference on Earthquake, Santiago, Chile, January 9–13, 2017.

25. M. C. Griffith, J. Vaculik, N. T. K. Lam, J. Wilson, and E. Lumantarna, "Cyclic Testing of Unreinforced Masonry Walls in Two-Way Bending," *Earthquake Engineering & Structural Dynamics* 36, no. 6 (2007): 801–821, https://doi.org/10.1002/eqe.654.

26. P. Padalu, Y. Singh, and S. Das, "Cyclic Two-Way Out-of-Plane Testing of Unreinforced Masonry Walls Retrofitted Using Composite Materials," *Construction and Building Materials* 238 (2020): 117784, https://doi.org/10.1016/j.conbuildmat.2019.117784.

27. M. Damiola, R. Esposito, F. Messali, and J. G Rots, "Quasi-Static Cyclic Two-Way Out-of-Plane Bending Tests and Analytical Models Comparison for URM Walls," paper presented at the *10th International Masonry Conference*, Milan, Italy, July 9–11, 2018.

28. M. Tondelli, K. Beyer, and M. DeJong, "Influence of Boundary Conditions on the Out-of-Plane Response of Brick Masonry Walls in Buildings With RC Slabs," *Earthquake Engineering & Structural Dynamics* 45, no. 8 (2016): 1337–1356, https://doi.org/10.1002/eqe.2710.

29. O. Penner and K. J. Elwood, "Out-of-Plane Dynamic Stability of Unreinforced Masonry Walls in One-Way Bending: Parametric Study and Assessment Guidelines," *Earthquake Spectra* 32, no. 3 (2016): 1699–1723, https://doi.org/10.1193/011715EQS011M.

30. S. Sharma, U. Tomassetti, F. Graziotti, and G. Magenes, "Simplified Methodologies for Assessing the Out-of-plane Two-Way Bending Seismic Response of Unreinforced Brick Masonry Walls: Lessons From Recent Experimental Studies," *Structures* 33 (2021): 2839–2854, https://doi.org/10.1016/j.istruc.2021.03.121.

31. U. Tomassetti, A. A. Correia, P. X. Candeias, F. Graziotti, and A. Campos Costa, "Two-Way Bending Out-of-Plane Collapse of a Full-Scale URM Building Tested on a Shake Table," *Bulletin of Earthquake Engineering* 17, no. 4 (2019): 2165–2198, https://doi.org/10.1007/s10518-018-0507-5.

32. L. Chang, F. Messali, and R. Esposito, "Capacity of Unreinforced Masonry Walls in Out-of-Plane Two-Way Bending: A Review of Analytical Formulations," *Structures* 28 (2020): 2431–2447, https://doi.org/10.1016/j.istruc.2020.10.060.

33. P. Kesavan and A. Menon, "A Macro-Element With Bidirectional Interaction for Seismic Analysis of Unreinforced Masonry Walls," *Earthquake Engineering & Structural Dynamics* 52, no. 6 (2023): 1740–1761, https://doi.org/10.1002/eqe.3841.

34. P. B. Lourenço, "Anisotropic Softening Model for Masonry Plates and Shells," *Journal of Structural Engineering* 126 (2000): 1008–1016.

35. S. Noor-E-Khuda, "An Explicit Finite-Element Modeling Method for Masonry Walls Using Continuum Shell Element," *Journal of Architectural Engineering* 27, no. 4 (2021): 1–15, https://doi.org/10.1061/(ASCE)AE.1943-5568.0000518.

36. S. Noor-E-Khuda, M. Dhanasekar, and D. P. Thambiratnam, "An Explicit Finite Element Modelling Method for Masonry Walls Under Out-of-Plane Loading," *Engineering Structures* 113 (2016): 103–120, https://doi.org/10.1016/j.engstruct.2016.01.026.

37. R. G. Selby and F. J. Vecchio, *Three-dimensional Constitutive Relations for Reinforced Concrete* (University of Toronto, 1993).

38. J. G. Rots, F. Messali, R. Esposito, S. Jafari, and V. Mariani, "Thematic Keynote Computational Modelling of Masonry With a View to Groningen Induced Seismicity," paper presented at the 10th International Conference on Structural Analysis of Historical Constructions, Leuven, Belgium, (September 10–15, 2016).

39. S. Sharma, L. C. Silva, F. Graziotti, G. Magenes, and G. Milani, "Modelling the Experimental Seismic Out-of-Plane Two-Way Bending Response of Unreinforced Periodic Masonry Panels Using a Non-Linear Discrete Homogenized Strategy," *Engineering Structures* 242 (2021): 112524, https://doi.org/10.1016/j.engstruct.2021.112524.

40. A. Mohyeddin, H. M. Goldsworthy, and E. F. Gad, "FE Modelling of RC Frames With Masonry Infill Panels Under In-Plane and Out-of-Plane Loading," *Engineering Structures* 51 (2013): 73–87, https://doi.org/10.1016/j.engstruct.2013.01.012.

41. P. Kesavan and A. Menon, “Investigation of In-Plane and Out-of-Plane Interaction in Unreinforced Masonry Piers by Block-Based Micro-Modeling,” *Structures* 46 (2022): 1327–1344, https://doi.org/10.1016/j.istruc.2022.10.105.

42. A. M. D’Altri, S. de Miranda, G. Castellazzi, and V. Sarhosis, “A 3D Detailed Micro-Model for the In-Plane and Out-of-Plane Numerical Analysis of Masonry Panels,” *Computers & Structures* 206 (2018): 18–30, https://doi.org/10.1016/j.compstruc.2018.06.007.

43. Z. Xie, M. Sousamli, F. Messali, and J. G. Rots, “A Sub-Stepping Iterative Constitutive Model for Cyclic Cracking-Crushing-Shearing in Masonry Interface Elements,” *Computers & Structures* 257 (2021): 106654, https://doi.org/10.1016/j.compstruc.2021.106654.

44. A. M. D’Altri, V. Sarhosis, G. Milani, et al., “Modeling Strategies for the Computational Analysis of Unreinforced Masonry Structures: Review and Classification,” *Archives of Computational Methods in Engineering* 27, no. 4 (2020): 1153–1185, https://doi.org/10.1007/s11831-019-09351-x.

45. Y. P. Oktiovan, F. Messali, B. Pulatsu, J. V. Lemos, and J. G. Rots, “A Contact-Based Constitutive Model for the Numerical Analysis of Masonry Structures Using the Distinct Element Method,” *Computers & Structures* 303 (2024): 107499, https://doi.org/10.1016/j.compstruc.2024.107499.

46. Y. Nie, A. Sheikh, P. Visintin, and M. Griffith, “A Robust Computational Strategy for Failure Prediction of Masonry Structures Using an Improved Multi-Surface Damage-Plastic Based Interface Model,” *International Journal for Numerical Methods in Engineering* 124, no. 11 (2023): 2498–2528, https://doi.org/10.1002/nme.7218.

47. L. Macorini and B. A. Izzuddin, “A Non-Linear Interface Element for 3D Mesoscale Analysis of Brick-Masonry Structures,” *International Journal for Numerical Methods in Engineering* 85, no. 12 (2011): 1584–1608, https://doi.org/10.1002/nme.3046.

48. A. M. D’Altri, F. Messali, J. Rots, G. Castellazzi, and S. de Miranda, “A Damaging Block-Based Model for the Analysis of the Cyclic Behaviour of Full-Scale Masonry Structures,” *Engineering Fracture Mechanics* 209 (2019): 423–448, https://doi.org/10.1016/j.engfracmech.2018.11.046.

49. A. Ghezelbash, A. M. D’Altri, S. Sharma, P. B. Lourenço, J. G. Rots, and F. Messali, “A Block-Based Numerical Strategy for Modeling the Dynamic Out-of-Plane Behavior of Unreinforced Brick Masonry Walls,” Meccanica (2024), https://doi.org/10.1007/s11012-024-01899-8.

50. F. Graziotti, U. Tomassetti, A. Penna, and G. Magenes, “Out-of-Plane Shaking Table Tests on URM Single Leaf and Cavity Walls,” *Engineering Structures* 125 (2016): 455–470, https://doi.org/10.1016/j.engstruct.2016.07.011.

51. S. Sharma, U. Tomassetti, L. Grottoli, and F. Graziotti, “Two-way Bending Experimental Response of URM Walls Subjected to Combined Horizontal and Vertical Seismic Excitation,” *Engineering Structures* 219 (2020): 110537, https://doi.org/10.1016/j.engstruct.2020.110537.

52. U. Tomassetti, L. Grottoli, S. Sharma, and F. Graziotti, “Dataset From Dynamic Shake-Table Testing of Five Full-Scale Single Leaf and Cavity URM Walls Subjected to Out-of-Plane Two-Way Bending,” *Data in Brief* 24 (2019): 103854, https://doi.org/10.1016/j.dib.2019.103854.

53. S. Sharma, L. Grottoli, U. Tomassetti, and F. Graziotti, “Dataset From Shake-Table Testing of Four Full-Scale URM Walls in a Two-Way Bending Configuration Subjected to Combined Out-of-Plane Horizontal and Vertical Excitation,” *Data in Brief* 31 (2020): 105851, https://doi.org/10.1016/j.dib.2020.105851.

54. F. Graziotti, A. Penna, and G. Magenes, “A Comprehensive In Situ and Laboratory Testing Programme Supporting Seismic Risk Analysis of URM Buildings Subjected to Induced Earthquakes,” *Bulletin of Earthquake Engineering* 17, no. 8 (2019): 4575–4599, https://doi.org/10.1007/s10518-018-0478-6.

55. S. Sharma, U. Tomassetti, L. Grottoli, and F. Graziotti, *Out-of-Plane Two-Way Bending Shaking Table Tests on Single Leaf and Cavity Walls (Report EUC137/2018U)* (EUCENTRE, University of Pavia, Pavia, Italy, 2018).

56. S. Kallioras, F. Graziotti, and A. Penna, “Numerical Assessment of the Dynamic Response of a URM Terraced House Exposed to Induced Seismicity,” *Bulletin of Earthquake Engineering* 17, no. 3 (2019): 1521–1552, https://doi.org/10.1007/s10518-018-0495-5.

57. F. Graziotti, U. Tomassetti, S. Kallioras, A. Penna, and G. Magenes, “Shaking Table Test on a Full Scale URM Cavity Wall Building,” *Bulletin of Earthquake Engineering* 15, no. 12 (2017): 5329–5364, https://doi.org/10.1007/s10518-017-0185-8.

58. J. J. Bommer, H. Crowley, R. Pinho, and B. Polidoro, *Selection of Acceleration Time-Series for Shake Table Testing of Groningen Masonry Building at the EUCENTRE, Pavia* (Groningen Field Seismic Hazard and Risk Assessment Project, 2015).

59. J. Yue, A. Fafitis, and J. Qian, “On the Kinematic Coupling of 1D and 3D Finite Elements: A Structural Model,” *Interaction and Multiscale Mechanics* 3, no. 2 (2010): 192–211, https://doi.org/10.12989/imm.2010.3.2.192.

60. D. M. Boore and J. J. Bommer, “Processing of Strong-Motion Accelerograms: Needs, Options and Consequences,” *Soil Dynamics and Earthquake Engineering* 25, no. 2 (2005): 93–115, https://doi.org/10.1016/j.soildyn.2004.10.007.

61. J. Lubliner, J. Oliver, S. Oller, and E. Oñate, “A Plastic-Damage Model for Concrete,” *International Journal of Solids and Structures* 25, no. 3 (1989): 299–326, https://doi.org/10.1016/0020-7683(89)90050-4.

62. J. Lee and G. L. Fenves, “Plastic-Damage Model for Cyclic Loading of Concrete Structures,” *Journal of Engineering Mechanics* 124, no. 8 (1998): 892–900, https://doi.org/10.1061/(ASCE)0733-9399(1998)124:8(892).

63. S. Jafari and R. Esposito, *Material Tests for the Characterisation of Replicated Calcium Silicate Brick Masonry* (Delft University of Technology, 2016).

64. G. Milani, M. Valente, and C. Alessandri, “The Narthex of the Church of the Nativity in Bethlehem: A Non-Linear Finite Element Approach to Predict the Structural Damage,” *Computers & Structures* 207 (2018): 3–18, https://doi.org/10.1016/j.compstruc.2017.03.010.

65. J. Scacco, B. Ghiassi, G. Milani, and P. B. Lourenço, “A Fast Modeling Approach for Numerical Analysis of Unreinforced and FRCM Reinforced Masonry Walls Under Out-of-Plane Loading,” *Composites Part B: Engineering* 180 (2020): 107553, https://doi.org/10.1016/j.compositesb.2019.107553.

66. H. M. Hilber, T. J. Hughes, and R. L. Talor, “Improved Numerical Dissipation for Time Integration Algorithms in Structural Dynamics,” *Earthquake Engineering and Structural Dynamics* 5, no. 3 (1977): 283–292.

67. A. J. Aref and K. M. Dolatshahi, “A Three-dimensional Cyclic Meso-Scale Numerical Procedure for Simulation of Unreinforced Masonry Structures,” *Computers and Structures* 120 (2013): 9–23, https://doi.org/10.1016/j.compstruc.2013.01.012.

68. N. Khattak, H. Derakhshan, D. P. Thambiratnam, D. Malomo, and N. J. Perera, “Modelling the In-Plane/Out-of-Plane Interaction of Brick and Stone Masonry Structures Using Applied Element Method,” *Journal of Building Engineering* 76 (2023): 107175, https://doi.org/10.1016/j.jobe.2023.107175.

69. S. Brzev and D. Anderson, *Seismic Design Guide for Masonry Buildings* (Canadian Concrete Masonry Producers Association, 2018).